Energy &
Environmental
Science

Quasi-Double-Star Nickel and Iron Active Sites for High-Efficient Carbon Dioxide Electroreduction

Journal:	*Energy & Environmental Science*
Manuscript ID	EE-ART-05-2021-001592
Article Type:	Paper
Date Submitted by the Author:	25-May-2021
Complete List of Authors:	Zhang, Ting; Catalan Institute of Nanoscience and Nanotechnology Han, Xu; Catalan Institute of Nanoscience and Nanotechnology Liu, Hong; ShanghaiTech University, Biset-Peiró, Martí; IREC Catalonia Institute for Energy Research, Department of Advanced Materials for Energy Zhang, Xuan; KU Leuven Tan, Pingping; Southwest University Chongqing Institute of Clean Energy and Advanced Materials Tang, Pengyi; Research Centre Jülich, Ernst Ruska-Centre for Microscopy and Spectroscopy with Electrons; Shanghai Institute of Microsystem and Information Technology, Zheng, Lirong; Institute of High Energy Physics, BSRF Yang, Bo; ShanghaiTech University, School of Physical Science and Technology Morante, Joan; IREC, advanced materials for energy Arbiol, Jordi; Institut Català de Nanociència i Nanotecnologia (ICN2), CSIC and The Barcelona Institute of Science and Technology (BIST), Advanced Electron Nanoscopy (GAeN); ICREA,

ARTICLE

Quasi-Double-Star Nickel and Iron Active Sites for High-Efficient Carbon Dioxide Electroreduction

Received 00th January 20xx,
Accepted 00th January 20xx

DOI: 10.1039/x0xx00000x

Ting Zhang,[a,b] Xu Han,[a] Hong Liu,[c] Martí Biset-Peiró,[b] Xuan Zhang,[d,e] Pingping Tan,[e] Pengyi Tang,*[f,g] Bo Yang,[c] Lirong Zheng,*[h] Joan Ramon Morante,[b,i] and Jordi Arbiol*[a,j]

Although the Faraday efficiencies (FEs) obtained on most of the Ni based single-atom catalysts (Ni-N-C) are satisfactory (generally > 90 %) for electrochemical transfer CO_2 to CO, the practical application is still limited by their high overpotentials (> 600 mV vs. RHE), which implies a higher consumption of energy to drive the CO_2 RR. In this work, we have prepared a quasi-double star catalyst composed of adjacent Ni and Fe active sites through a simple pyrolysis of Ni and Fe co-doped Zn-based MOFs in order to achieve a high selectivity at a low overpotential during CO_2 RR. Specifically, the optimized Ni/Fe-N-C catalyst shows an exclusive selectivity (a maximum FE (CO) of 98 %) at a low overpotential of 390 mV vs. RHE, which is superior to both single metal counterparts (Ni-N-C and Fe-N-C catalysts) and other state-of-the-art M-N-C catalysts. DFT results further reveal that regulating the catalytic CO_2 RR performance via adjacent Ni and Fe active sites can potentially break the activity benchmark of single metal counterparts because the neighboring Ni and Fe active sites not only function in synergy to decrease the reaction barrier for the formation of COOH* and desorption of CO* in comparison to their single metal counterparts, but also prevent the undesired hydrogen evolution reaction (HER). This work presents a quasi-double-star catalyst composed of two metal sites for high-efficient CO_2 reduction, which paves the way for the rational design of bimetallic catalysts with separated active sites for other reactions.

Introduction

Severe environmental problems have triggered the development of the electrochemical CO_2 reduction reaction (CO_2 RR) in order to mitigate the high atmospheric CO_2 concentration at ambient conditions and allow the production of useful and added value chemicals (e.g. CO, HCOOH, CH_4, CH_3CH_2OH).[1, 2] However, the efficiency of CO_2 RR is far from satisfactory due to the inherent inertness of CO_2 molecules and the parallel presence of the competitive hydrogen evolution reaction (HER) during the electrocatalytic processes.[3-5] Therefore, many research works have been devoted to design cost-friendly electrocatalysts for achieving a high CO_2 conversion efficiency.

As a frontier in materials science, single-atom catalysts (SACs) with a higher density of exposed catalytic sites at an atomic level, have recently emerged, showing a great potential in the field of CO_2 RR, due to their high selectivity and suppression of the competing HER.[6-10] Typically, Ni-based SACs have been the focus of interest for the CO generation because of their high Faradaic efficiencies (FEs).[11-15] For example, Wen et al. reported that Ni-N-C catalysts exhibited an excellent CO_2 RR performance with a FE for CO over 99 % at −0.80 V vs. RHE.[16] A Ni single-atom catalyst loaded in a hollow mesoporous carbon sphere was fabricated by Xiong et al., delivering a high CO_2 RR selectivity (FE(CO) of 95 %) at −0.90 vs. RHE.[17] It is well established that most of the Ni-N-C catalysts possess a high selectivity. However, as a counterpart, they usually show a high overpotential (generally > 600 mV vs. RHE), which is derived from their sluggish kinetics on Ni-N sites during the first proton-coupled electron transfer ($CO_2 + H^+ + e^- \rightarrow COOH^*$).[18, 19] These high overpotentials necessitate more energy to drive the CO_2 RR than that thermodynamically needed.[20, 21] In light of this, researchers spared no effort in optimizing the Ni-N-C catalysts to achieve a high FE(CO) at a

---

[a] *Catalan Institute of Nanoscience and Nanotechnology (ICN2), CSIC and BIST, Campus UAB, Bellaterra, Barcelona, 08193, Catalonia, Spain E-mail: arbiol@icrea.cat*
[b] *Catalonia Institute for Energy Research (IREC), Jardins de les Dones de Negre 1, Sant Adrià del Besòs, Barcelona, 08930, Catalonia, Spain*
[c] *School of Physical Science and Technology, ShanghaiTech University, 393 Middle Huaxia Road, Shanghai, 201210, P. R. China*
[d] *Department of Materials Engineering, KU Leuven, Kasteelpark Arenberg, 44, B-3001 Leuven, Belgium*
[e] *Institute for Clean Energy & Advanced Materials, Faculty of Materials & Energy, Southwest University, Chongqing 400715, China*
[f] *Ernst Ruska-Centre for Microscopy and Spectroscopy with Electrons and Peter Grünberg Institute, Forschungszentrum Jülich GmbH, Jülich, 52425, Germany*
[g] *Institute of Microsystem and Information Technology, Chinese Academy of Sciences, Shanghai, 200050, P. R. China E-mail: py.tang@mail.sim.ac.cn*
[h] *Beijing Synchrotron Radiation Facility, Institute of High Energy Physics, Chinese Academy of Sciences, Beijing, 100049, P. R. China E-mail: zhenglr@ihep.ac.cn*
[i] *Department of Physics, Universitat de Barcelona, Barcelona, 08028, Catalonia, Spain*
[j] *ICREA, Pg. Lluís Companys 23, Barcelona, 08010, Catalonia, Spain E-mail: arbiol@icrea.cat*

† Footnotes relating to the title and/or authors should appear here.

Electronic Supplementary Information (ESI) available: [details of any supplementary information available should be included here]. See DOI: 10.1039/x0xx00000x low overpotential, thus, meeting the requirements of practical applications.[22-24]

In order to improve the catalytic activity on Ni-N-C catalysts, one direct method is to optimize the first reaction step to obtain a high performance in the overall CO_2-to-CO conversion process. In this way, 'tandem catalysis' is considered as one of the most inspiring strategies to break the linear scaling relations of the adsorption and desorption of reaction intermediates on the different active sites, thus, leading to an unprecedented catalytic ability.[10, 25-27] Moreover, the electronic interactions and configuration environment between two active sites would be regulated and hence influence their synergistic catalytic performance.[28-31] For instance, in comparison to metal single-atom sites, the formed double-metal active sites with their configuration structures can not only facilitate the O_2 adsorption, but also weak the O=O bonds, thus, boosting the efficiency of the oxygen reduction reaction (ORR).[30, 32, 33] With this in mind, we propose that a bimetallic catalyst should hold the potential for high efficiency CO_2 RR, although such double metal-atom catalysts are still in their infancy towards CO_2 RR.[10]

In the present work, we have combined the advantages of both Ni-N-C and Fe-N based catalysts. Herein, we have prepared a quasi-double-star Ni/Fe catalyst, aiming to achieve a high selectivity at a low overpotential during CO_2 RR. On one hand, Ni-N-C catalysts possess a rapid desorption of *CO ($CO^* \rightarrow CO + ^*$) due to weak bonding of CO, whereas Fe-N active sites generally show a low overpotential for CO_2 RR because of the fast first proton-coupled electron transfer.[19] The cooperation of closely positioned Fe and Ni active sites in a catalyst might act as a nano-reactor, and significantly, affect different reaction steps on the two separated active sites, enhancing the CO_2 RR activity and selectivity. In addition, the presence of Fe adjacent to the Ni sites in a specific environment could influence the electron density and configuration environment between both active sites, and thus facilitate the adsorption and desorption of intermediates in the CO_2 reduction process.[33] Specifically, via a one-pot solvothermal synthesis, instead of a tedious multi-step doping process, we have prepared ternary metal-organic frameworks (MOFs) by rationally controlling Ni and Fe additive amounts in Zn-based IRMOF-3. Then, the adjacent Ni and Fe double active sites formed via a simple pyrolysis. As a result, the optimized Ni_7/Fe_3-N-C sample shows an excellent selectivity to CO evolution (FE_{CO} is 98 %) at a low overpotential (390 mV vs. RHE), which are superior to both single metal counterparts (Ni-N-C and Fe-N-C catalysts) and other state-of-the-art single/double atom catalysts. Meanwhile, DFT results reveal that compared to Ni-N-C catalysts, this bimetallic catalyst with neighbouring Ni and Fe sites could facilitate the formation of COOH*. Moreover, the Ni/Fe-N-C catalyst not only could boost the desorption of CO*, but also limit the undesired HER in comparison to Fe-N-C, thus, leading to a win-win activity towards CO_2 RR. Consequently, the excellent catalytic activity is attributed to the synergistic effect between the adjacent Ni and Fe active sites, which play an important role in regulating the binding energy of different intermediates during the adsorption and desorption processes, influencing different reaction steps towards CO_2 RR. This work not only demonstrates that the catalysts with adjacent double-metal single atoms are promising electrocatalysts for CO_2 RR, but also proves that such double metal sites can perfectly work as a nano-reactor, influencing different reaction steps on different active sites.

Results and discussion

Synthesis and Characterizations of Different Catalysts

The Ni/Fe-N-C sample was synthesized using a two-step procedure, as shown in Fig. 1c. First, a Ni and Fe co-doped Zn-IRMOF-3 was prepared by a simple one-pot solvothermal method. For comparison, single metal (Fe or Ni) doped-Zn-IRMOF-3 was also synthesized through the same method only containing Fe or Ni salt solutions (Fig. 1a and Fig. 1b). Afterwards, the Ni-N-C, Fe-N-C and Ni/Fe-N-C catalysts were obtained by a simple pyrolysis under Ar atmosphere. Detailed synthetic procedures can be found in the experimental section. X-ray diffraction (XRD) analysis indicates that the Ni and/or Fe-doped MOF precursors and IRMOF-3 possessed a similar crystal structure, according to their XRD patterns (Fig. S1).[34] Meanwhile, as shown in the Fourier transform infrared (FTIR) spectra (Fig. S2), compared to the pure IRMOF-3, the absence of obvious differences on the characteristic peaks proved that introducing Ni and/or Fe did not change the functional groups of IRMOF-3. Furthermore, the structures, morphologies and element distributions of the different precursors were studied by field emission scanning electron microscopy (FE-SEM), and transmission electron microscopy (TEM) measurements. As revealed by FE-SEM (Fig. S3), the as-prepared Ni_7/Fe_3-IRMOF-3 and the corresponding single M-IRMOF-3 exhibited a similar morphology, maintaining the initial spherical shapes of IRMOF-3. The representative high angle annular dark-field scanning transmission electron microscopy (HAADF STEM) images showed that the Fe-IRMOF-3, Ni-IRMOF-3 and Ni_7/Fe_3-IRMOF-3 catalysts exhibited

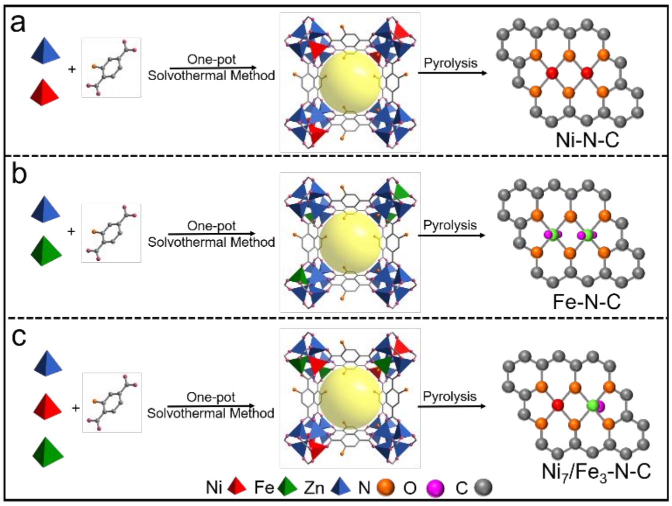

Fig. 1. Schematic illustration of the preparation process of (a) Ni-N-C, (b) Fe-N-C and (c) Ni_7/Fe_3-N-C samples.

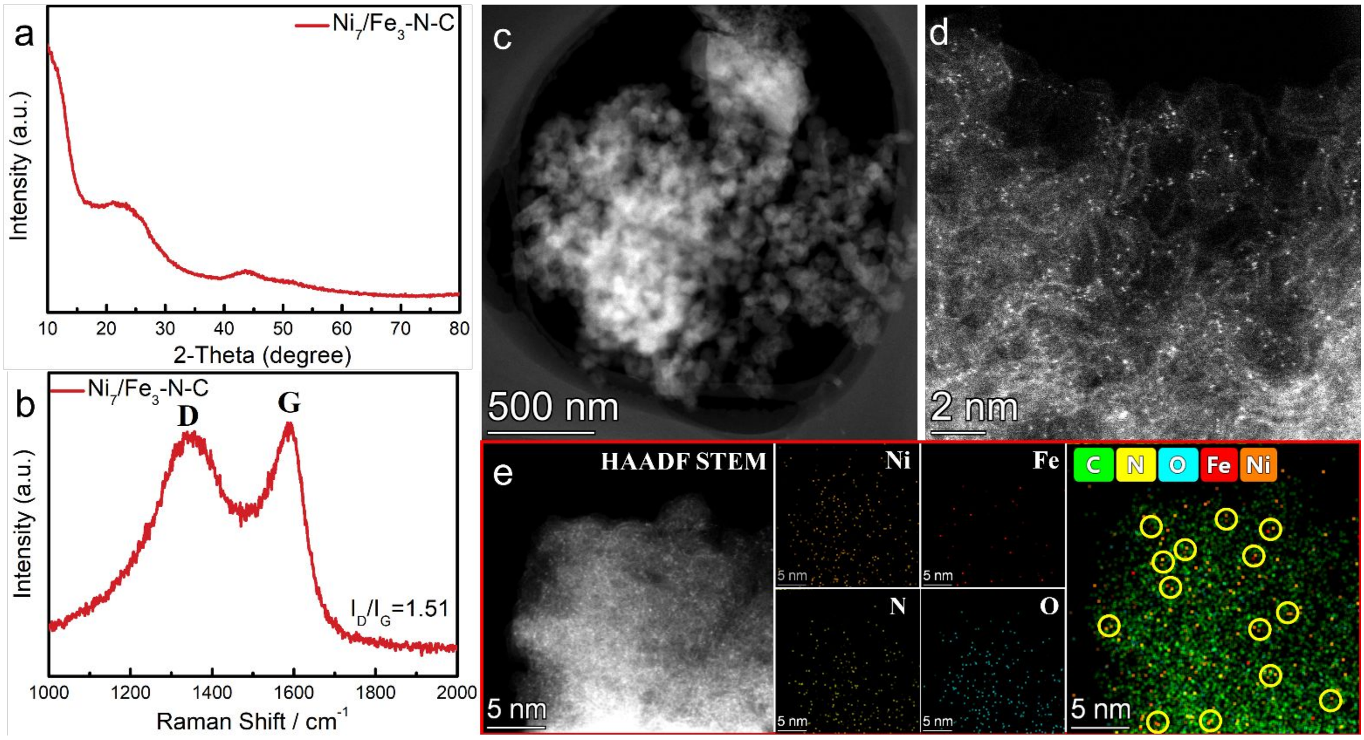

Fig. 2. Characterizations of Ni_7/Fe_3-N-C. (a) XRD patterns, (b) Raman spectra, (c) low magnification and (d) high magnification aberration-corrected HAADF STEM images, (e) HAADF STEM image and representative EDS chemical compositions of Ni_7/Fe_3-N-C sample.

spheroidal particle-shape structures (Fig. S4-S6). The elemental distribution of these materials was investigated by electron energy loss spectroscopy (EELS), demonstrating the uniform dispersions of C, N, O and Zn elements throughout all the samples. In addition, we also found a uniform distribution of Ni or/and Fe, when present, in the Ni-IRMOF-3, Fe-IRMOF-3 and Ni_7/Fe_3-IRMOF-3 samples. Fig. S7a shows the typical nitrogen isothermal adsorption/desorption curves for the different samples. Significantly, the prepared precursors exhibited the typical type IV N2 adsorption isotherm. In addition, the surface area values calculated by Brunauer-Emmett-Teller (BET) analyses suggest that the porosity of the initial IRMOF-3 remained almost intact after the introduction of the Ni and/or Fe species, suggesting that the pores were not filled by metallic precipitates or clusters, during the one-pot synthesis process (Fig. S7b). The pyrolysis process of the Ni_7/Fe_3-IRMOF-3 sample was tracked by thermogravimetric analysis (TGA) (Fig. S8).

After pyrolysis, the crystal structure of Ni-N-C, Fe-N-C and Ni_7/Fe_3-N-C catalysts was also analysed by XRD in Fig. S9 and Fig. 2a. Clearly, these three samples show similar diffraction patterns with two broad peaks at about 24° and 44°, representing the (002) and (100) diffraction planes for graphite carbon, which indicates the existence of a carbon matrix in these samples after pyrolysis.[35, 36] Moreover, the characteristic peaks of metal hybrids are absent in the XRD patterns of the pyrolyzed products. The Raman spectra of Ni-N-C, Fe-N-C and Ni_7/Fe_3-N-C samples are shown in Fig. 2b and Fig. S10, presenting two main peaks at around 1365 and 1590 cm^{-1} corresponding to the typical D and G bands of graphitic carbon. Compared to the Raman spectra of the pure Ni-N-C sample, the I_d/I_g band intensity ratio of Fe-N-C and Ni_7/Fe_3-N-C samples was slightly lower, suggesting a smaller number of defects and a higher extent of graphitization in these two samples.[37, 38]

Aberration corrected (AC) HAADF STEM analyses was used to determine the morphology, structure and element distribution in the Ni_7/Fe_3-N-C sample, as displayed in Fig. 2c-2e and Figs. S11-S12. Fig. 2c and Fig. S11a show that the as-prepared Ni_7/Fe_3-N-C is still composed of irregular shape nanoparticles, indicating that the pyrolysis process did not completely destroyed the pristine structure of the MOF precursors. More importantly, we could not observe the presence of small bright clusters in low magnification HAADF STEM images, revealing that there are no metal nanoparticles or cluster formed during the Ni_7/Fe_3-N-C catalyst formation process, which is consistent with the XRD results (Fig. 2a). AC HAADF STEM images (Fig. 2d and Fig. S11b-i) validate the presence of homogeneously distributed high density of metal single-atoms, directly proving that the Ni and Fe have successfully been introduced as atomic dispersion sites in the Ni_7/Fe_3-N-C sample. In addition, the elemental distribution was elucidated by energy dispersive X-ray spectroscopy (EDS), which not only revealed the homogeneous distribution of Ni, Fe, O and N dispersed in the whole carbon matrix (Fig. 2e and Fig. S12), but also clearly identified the existence of many neighbouring dual-dots marked by the yellow circles, suggesting the formation of adjacent Ni and Fe sites. These results indicate that neighbouring Ni and Fe sites could be successfully prepared, although few Ni or Fe individual sites also exist. In addition, the HAADF STEM images of Ni-N-C and Fe-N-C are shown in Figs. S13-S14. Multiple areas of the Ni-N-C sample were examined and no presence of Ni nanoparticles (precipitates) could be observed, proving that Ni atoms were also atomically

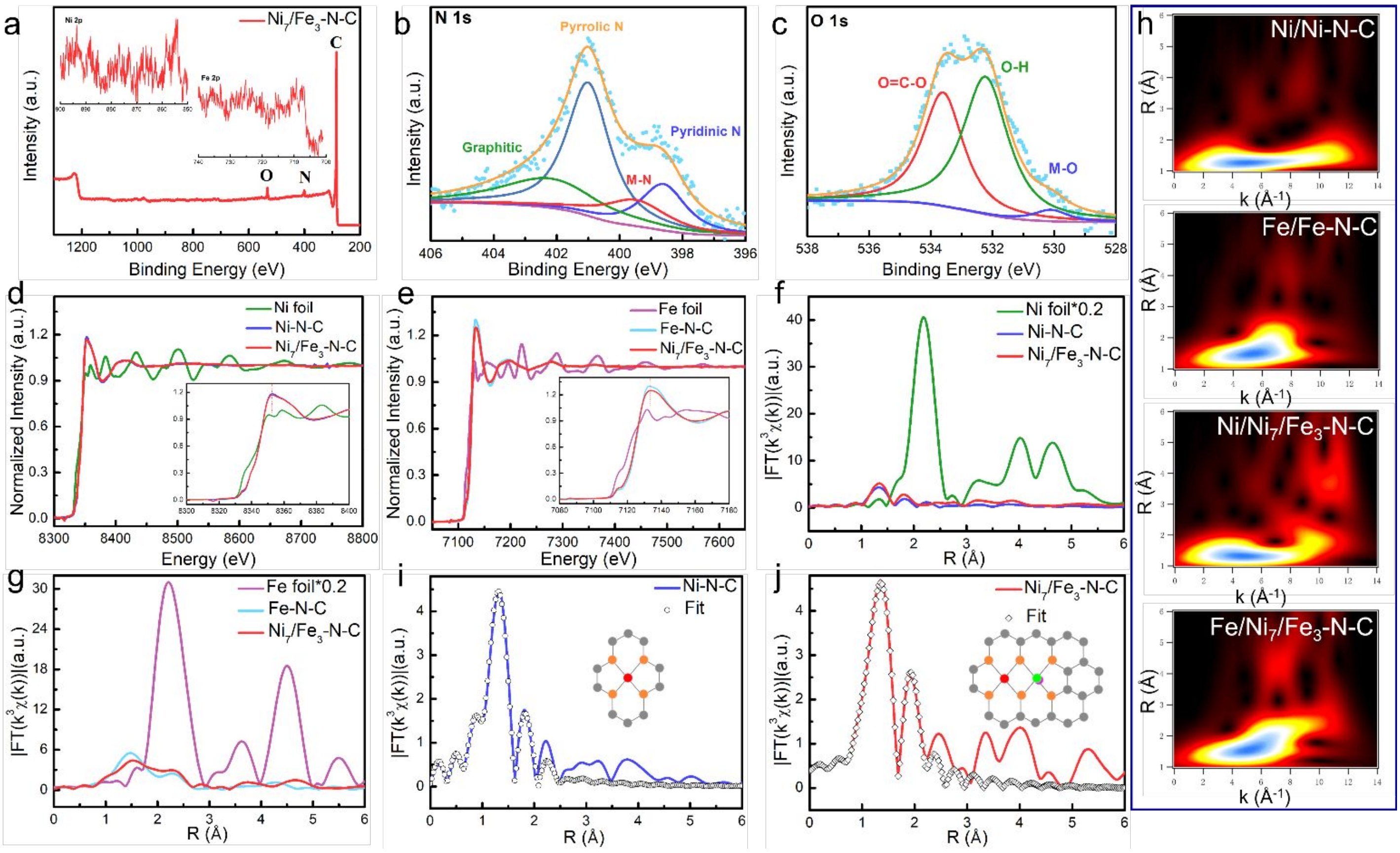

Fig. 3. Characterizations of Ni-N-C, Fe-N-C and Ni$_7$/Fe$_3$-N-C. (a) XPS spectra for the survey scan, (inset) Ni 2p and Fe 2p of Ni$_7$/Fe$_3$-N-C. (b) High-resolution XPS (b) N 1s and (c) O 1s spectrum of Ni$_7$/Fe$_3$-N-C. (d) XANES spectra of the Ni-N-C and Ni$_7$/Fe$_3$-N-C at Ni K-edge. The insets are the magnified corresponding regions. (e) XANES spectra of the Fe-N-C and Ni$_7$/Fe$_3$-N-C at Fe K-edge. The insets are the magnified corresponding regions. EXAFS spectra at (f) Ni K-edge and (g) Fe K-edge. (h) WT-EXAFS of Ni-N-C, Fe-N-C and Ni$_7$/Fe$_3$-N-C. The corresponding Ni K-edge EXAFS fitting parameters for (i) Ni-N-C and (j) Ni$_7$/Fe$_3$-N-C sample. (Ni, Fe, O, N, C atoms are represented in red, green, pink, orange and grey, respectively).

dispersed, in agreement with the XRD results. However, it is worth noting that some bulk Fe particles could be observed in Fig. S14a, indicating that a small partial Fe aggregation occurred in the Fe-N-C sample. Interestingly, the cyclic voltammetry (CV) curves in Fig. S15, did not show the typical Fe reduction/oxidation redox peaks in the Fe-N-C sample, which was similar to the result obtained for the Ni$_7$/Fe$_3$-N-C catalyst, suggesting that the Fe clusters could not directly contact the solution to react. This result is rationalized by the presence of a carbon shell over the Fe clusters as observed by HRTEM (Fig. S15c), which could cut off the reaction between Fe particles and the solution.[39]

X-ray photoelectron spectroscopy (XPS) was used to characterize the catalysts' surfaces and compositions. The full survey scan XPS spectrum of Ni$_7$/Fe$_3$-N-C shown in Fig. 3a indicates that only the elemental signals for C, N and O could be observed. Meanwhile, a similar phenomenon is observed in the full survey scan XPS spectrum for Ni-N-C and Fe-N-C catalysts, as shown in Fig. S16. The high-resolution N 1s spectrum (Fig. 3b and Fig. S17) of all samples can be deconvoluted into four components corresponding to pyridinic N (centred at 398.7 eV), pyrrolic N (401.0 eV), graphitic N (402.1 eV), and a porphyrin-like moiety at 399.5 eV corresponding to the metal-nitrogen (M-N) coordination.[19, 40] Notably, the high resolution O 1s spectroscopy deconvolution revealed the presence of the metal-O bond at 530 eV in Fe-N-C and Ni$_7$/Fe$_3$-N-C samples, potentially implying the retainment of M-O chelation after calcination because of the oxygen-rich IRMOF-3 precursors (Fig. 3c and Fig. S18).[41] To further uncover information on the local structure of the different samples, X-ray absorption spectroscopy (XAS) was performed at both Ni K-edge and Fe K-edge for Ni$_7$/Fe$_3$-N-C and the corresponding single M-N-C catalysts. The XANES K-edge characterization was used to explore the structure and valence of the metal in the active sites.[33] As shown in the Ni K-edge X-ray absorption near-edge structure (XANES) of a reference Ni foil, Ni-N-C and Ni$_7$/Fe$_3$-N-C (Fig. 3d), the Ni K-edge spectra of both Ni-N-C and Ni$_7$/Fe$_3$-N-C shift towards higher binding energy compared to that of the Ni foil, suggesting a positive charge state of Ni atoms in the as-prepared catalysts (Ni-N-C and Ni$_7$/Fe$_3$-N-C).[11] The insets of Fig. 3d and Fig. S19a highlight the pre-edge features at approximately 8334 eV, corresponding to the signals of 3d and 4p orbital hybridization of the Ni central atoms.[18] Meanwhile, the increased peak intensity in Ni$_7$/Fe$_3$-N-C, compared to the Ni-N-C, is ascribed to the distorted D_{4h} symmetry.[18, 42] These results certify that Ni species in Ni-N-C and Ni$_7$/Fe$_3$-N-C exhibit a similar coordination path between metal centres and pyridinic/pyrrolic N, but the D_{4h} symmetry in Ni$_7$/Fe$_3$-N-C is distorted by another coordination path such as the presence of a neighbouring Fe coordination, in good agreement with the dual bright dots observed in AC HAADF STEM and EDS images (Fig. 1e).[19] Similarly, Fig. 3e present the Fe K-edge spectra for the Ni$_7$/Fe$_3$-N-C catalyst along with the Fe foil reference and the Fe-N-C sample for comparison. Here, XANES clearly reveals that the Fe K-edge energy absorption threshold of Ni_7/Fe_3-N-C and Fe-N-C are different from the Fe foil reference, which indicates that the valence of Fe in Ni_7/Fe_3-N-C and Fe-N-C catalysts is higher than Fe^0.[43] Moreover, as shown in Fig. 3e inset, the presence of the pre-edge peak at around 7117 eV, which is the fingerprint of D_{4h} symmetry, can be attributed to the Fe-N square planar configuration and the existence of Fe-N (O, C) coordination in Ni_7/Fe_3-N-C and Fe-N-C catalysts.[44] Additional information is obtained from the Fourier transform (FT) k^2-weighted $\chi(k)$ function of the Ni K-edge EXAFS of Ni-N-C and Ni_7/Fe_3-N-C catalysts, as shown in Fig. 3f. The Ni-N-C and Ni_7/Fe_3-N-C spectra show a main peak at 1.35 Å corresponding to the Ni-N scattering path, which is quite different from that observed at the standard Ni foil at 2.2 Å assigned to the metal-metal path.[16, 19] From the Fourier transform (FT) k^2-weighted $\chi(k)$ function spectra of the Fe K-edge EXAFS of Fe-N-C and Ni_7/Fe_3-N-C catalysts (Fig. 3g), the main peaks at 1.5 Å stand for Fe-N(O, C) bonds, respectively.[21, 43] Meanwhile, there is no obvious metal-metal path for Ni_7/Fe_3-N-C, corroborating the absence of Ni-Fe, Ni-Ni or Fe-Fe coordination. Wavelet-transform (WT) plots (Fig. 3h) were conducted to further verify the coordination information of the Ni_7/Fe_3-N-C catalyst. One intensity maximum is present at about 4.0 $Å^{-1}$ in the Ni WT contour plots of the Ni-N-C and Ni_7/Fe_3-N-C catalysts, which can be assigned to the Ni-N pair.[3] The analysis results of the Fe WT contour plots for all the samples are similar to the Ni plots. Therefore, both the FT- and WT-EXAFS analyses demonstrate that Ni and Fe atoms are mainly present in the Ni_7/Fe_3-N-C sample as atomic dispersions. To verify the detailed atomic structure of Ni-N-C, Fe-N-C and Ni_7/Fe_3-N-C, we obtained their corresponding EXAFS spectra, as shown in Figs. 3i-3j and Fig. S20. According to the fitting results and the corresponding fitting parameters listed in Tables S1 and S2, the Ni-N coordination number for Ni_7/Fe_3-N-C and Ni-N-C catalysts are 4.5 and 3.9, with a corresponding bond length of 1.84 Å and 1.87 Å, respectively. These latest results suggest that most of the single Ni atoms are coordinated with four nitrogen atoms on the Ni_7/Fe_3-N-C and Ni-N-C samples. In addition, the optimized Fe K-edge EXAFS spectra fitting results for the Ni_7/Fe_3-N-C catalyst showed a CN-value of 4.8 and a mean bond length of 1.98 Å, suggesting that the Fe single atoms should coordinate with four N atoms and one O atom. Both experimentally and theoretically previous results show that metal-nitrogen bonds are more likely than the metal-carbon or metal-oxygen ones, suggesting to form in-plane FeN_4 sites in the first coordination sphere.[41, 45] However, the higher average CN-value in the Fe-N-C-based material strongly suggests that one axial O atom is adsorbed on top of the FeN_4 moieties, resulting in coordinatively saturated iron cations, in line with the high oxophilicity of Fe.[41, 45, 46] Meanwhile, the formed HO-FeN_4 active sites could induce a rapid CO* desorption and suppress the competitive HER, resulting in an improved catalytic performance in comparison to that of the FeN_4 sites without axial O ligand.[47] Therefore, in an atmosphere with the oxygen-rich ligand, the spectra obtained on the Ni_7/Fe_3-N-C sample are fitted as presenting adjacent NiN_4 and HO-FeN_4 sites.

CO_2 RR in H-type Cell

The electrochemical CO_2 reduction activity of the as-prepared catalysts was assessed using a typical three-electrode H-cell separated by an anion exchange membrane in 0.5 M $NaHCO_3$ electrolyte. The gas products were regularly examined by online gas chromatography (GC), showing that CO and H_2 were the main gas products obtained for all the samples. In parallel, the liquid-phase products were analysed by using nuclear magnetic resonance (^{1}H-NMR) spectroscopy after the electrochemical CO_2 reduction processes, demonstrating there no liquid products were produced (Fig. S21).

In Fig. S22, we evaluate the CO_2 reduction performance of different MOF precursors. These MOF precursors showed an insufficient ability towards CO_2 RR to CO and a high performance for producing H_2. After pyrolysis, we firstly obtained CV curves to roughly assess the double/single M-N-C samples towards CO_2 RR. As shown in Fig. S23, these samples exhibited an increase of current density in CO_2-saturated solution, compared to those obtained in the Ar-saturated electrolyte, which confirmed the efficient catalytic performance of Ni-N-C, Fe-N-C and Ni_7/Fe_3-N-C samples.[14] Then, the catalytic activities for CO_2 RR were further investigated by the chronoamperometry method in CO_2-saturated 0.5 M $NaHCO_3$ solution. Fig. 4a summarizes the measured total current density for Ni-N-C, Fe-N-C and Ni_7/Fe_3-N-C samples. With the same mass loading of catalysts (ca. 1 mg cm^{-2}), the Ni-N-C delivers the smallest current density on each applied potential, which is lower than those obtained by the Fe-N-C and Ni_7/Fe_3-N-C samples. The result in Fig. 4a reveals that Ni-N-C exhibits a relatively poor activity for generating a current density (j). The corresponding FE for CO production is measured in a potential range from −0.40 to −0.70 V (vs. RHE) for all the catalysts synthesized, as shown in Fig. 4b. CO was the dominant gas product for these single/double M-N-C catalysts. Moreover, the FEs of the products varied with the electrode applied potentials. Specifically, the FE(CO) for the Fe-N-C and Ni_7/Fe_3-N-C catalysts typically exhibited an increase from ca. −0.40 to −0.50 V vs. RHE, reaching a maximum FE(CO) (90 % and 98 %, respectively) at −0.50 V vs. RHE. As the potential changed to more negative values (−0.6 to −0.7 V vs. RHE), the FEs(CO) for Fe-N-C and Ni_7/Fe_3-N-C gradually decreased since the competitive HER became the dominant reaction, as evidenced in the FE (H_2) shown in Fig. 4d. However, the FE(CO) of Ni-N-C increased dramatically as the potentials were getting more negative, until reaching the maximum FE (CO) (nearly 100 %) at −0.70 V vs. RHE. Accordingly, the obtained FEs of CO can be ranked in the following order: Ni_7/Fe_3-N-C > Fe-N-C > Ni-N-C in the potential range from −0.40 V to −0.50 V vs. RHE. Instead, when the potential is more negative than −0.60 V vs. RHE, the selectivity for CO follows the order: Ni-N-C > Ni_7/Fe_3-N-C > Fe-N-C. As discussed, the overpotential at the maximum FE for CO formation is crucial for catalysts in electrocatalysis, as it represents the energy that is required to drive the reaction

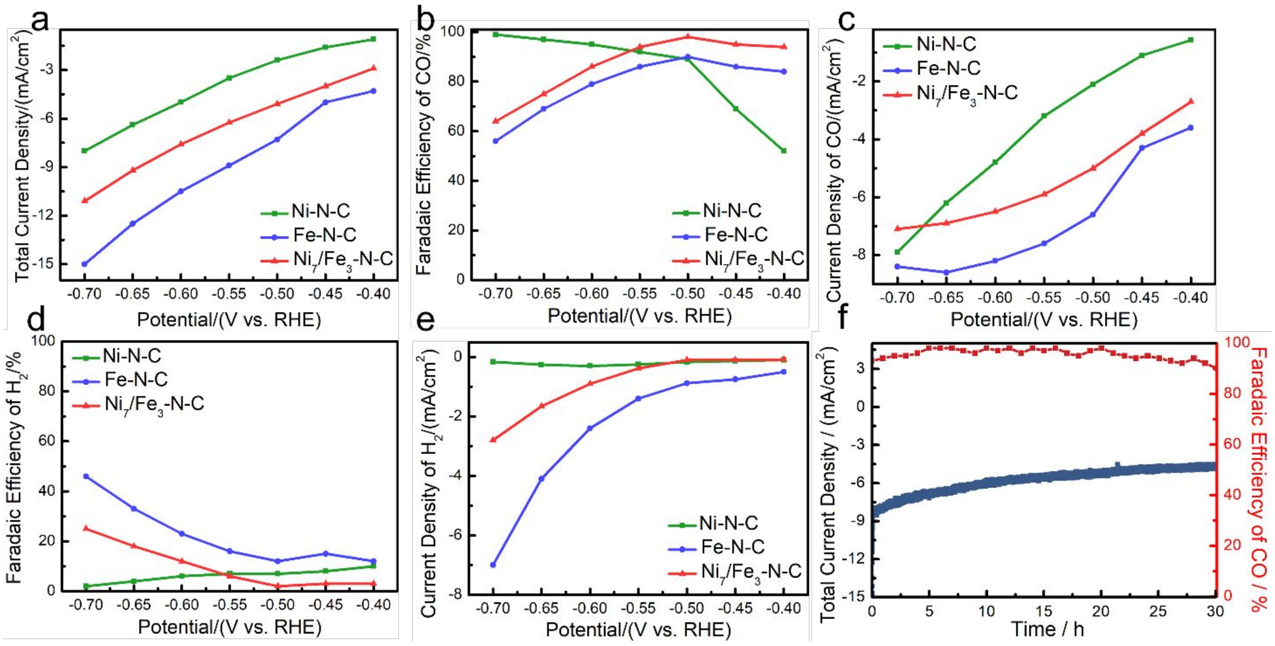

Fig. 4. Electrocatalytic Performance of CO_2 Reduction. (a) Total current density, (b) FE of CO at various potentials, (c) current density for CO production, (d) FE of H_2 at various potentials, (e) current density for H_2 production on Ni-N-C, Fe-N-C and Ni_7/Fe_3-N-C samples. (f) Stability test of Ni_7/Fe_3-N-C at −0.50 V vs. RHE.

beyond the one that is thermodynamically needed.[24] Among these catalysts, Ni_7/Fe_3-N-C exhibited the highest selectivity for CO production at −0.50 V (vs. RHE), corresponding to an overpotential of just 390 mV vs. RHE, which is lower than that of Ni-N-C as well as the majority of other reported Ni-N-C catalysts (see Table S3 in supporting information). Furthermore, Ni_7/Fe_3-N-C shows a partial current density for CO production of −5 mA cm^{-2} at −0.50 V (Fig. 4c). Meanwhile, the partial current density for CO production obtained by Ni7/Fe3-N-C is also significantly higher compared to the one obtained by Fe-N-C and Ni-N-C catalysts at most of the applied potentials. The potential-dependent H_2 current densities for the different catalysts are shown in Fig. 4e. Based on these results, it is shown that the bimetallic Ni_7/Fe_3-N-C produces a high-efficient CO_2 RR with a high selectivity and enhanced current densities at a low overpotential, results that are much better than those presented by the Ni-N-C sample. In order to further probe the high efficiency of Ni_7/Fe_3-N-C sample, we have estimated the electrochemical active surface areas (ECSA) of all samples and corresponding MOF precursors from the double-layer capacitance (C_{dl}) (Fig. S24). It is well established that higher ECSA often leads to higher catalytic activity.[48, 49] Compared to the MOF precursors, the samples after pyrolysis exhibited the smaller C_{dl}. This phenomenon suggests that the intrinsic catalytic activity of these M-N-C samples is not correlated to a higher ECSA. Instead, the improved CO_2 RR catalytic properties of these catalysts must be due to the presence of exposed isolated double or single metal active sites. The latest was further supported by the results obtained in a designed poisoning experiment with NaSCN solution. As shown in Fig. S25, the significant decrease of catalytic activity for Ni-N-C, Fe-N-C and Ni_7/Fe_3-N-C samples observed in $NaHCO_3$ solution containing NaSCN, could be attributed to the high affinity of SCN$^-$ to metal ions poisoning the single/double active sites. Meanwhile, Ni-N-C, Fe-N-C and Ni_7/Fe_3-N-C samples showed a similar C_{dl} (~16 mF cm^{-2}). The small difference in their ECSAs further proves that the adjacent Ni and Fe active sites in Ni_7/Fe_3-N-C significantly dominated the CO_2 RR process compared to the two single metal counterparts.[19] In addition, Nyquist plots revealed that the double/single M-N-C had a lower interfacial charge-transfer resistance (R_{CT}) compared to the MOF precursors, revealing faster electron transfer during CO_2 RR process, which is favourable for the formation of intermediates (Fig. S26).[16, 19, 39] Furthermore, the concentration effect of $NaHCO_3$ in the CO_2 RR on the Ni_7/Fe_3-N-C catalyst was also investigated (Fig. S27). The plot of log (j_{CO}) versus log ([HCO_3^-]) at the constant potential of −0.50 V vs. RHE showed a slope of 0.71, indicating that the concentration effect of HCO_3^- played a considerable role in promoting the conversion reaction of CO_2 to CO.[39, 50] Therefore, the HCO_3^- not only acts as a pH buffer and proton donor in this reaction, but also increases the concentration of CO_2 near the electrode surface.[39, 50, 51] In addition, by systematically controlling the ratio of Ni and Fe dopants, a series of Ni_x/Fe_y-N-C catalysts engaging both Ni and Fe sites were synthesized. We studied the electrochemical FEs on different Ni_x/Fe_y-N-C samples, as shown in Fig. S28. Specifically, Ni_x/Fe_y-N-C with a higher Ni dose still kept the high selectivity, but at a larger overpotential; however, Ni_x/Fe_y-N-C with a higher Fe dose showed a similar selectivity at the same applied potential compared with the single Fe-N-C catalyst. These results demonstrate that the presence of a certain amount of Fe single atoms indeed influences the generation of CO at different applied potentials. Similarly, a Ni_7/Co_3-N-C sample was fabricated by following the same methodology. However, it exhibited higher catalytic performance towards H_2 generation, as shown in Fig. S29. This result further reveals the dependence of the electrocatalytic performance on the introduction of different metals that are adjacent to the Ni sites. Because the secondary metal introduction determines

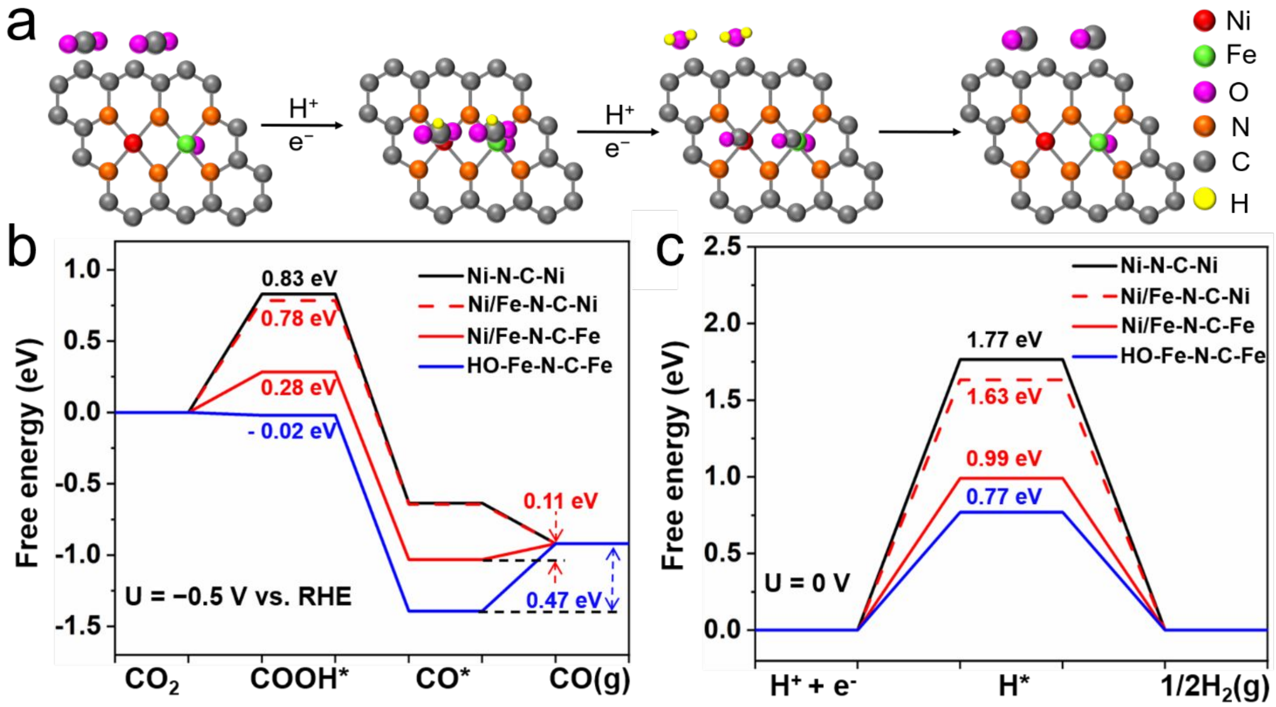

Fig. 5. DFT Studies of CO_2 RR. (a) Supposed pathway of CO_2 reduction to CO in DFT calculations. Free energy profiles for the (b) CO_2 RR to CO at −0.50 V (vs. RHE) and (c) HER at 0 V (vs. RHE) on simulated models.

the adsorption properties and surface reactivity of the bimetallic catalysts through the tuning of the electron environment, thus, influencing the activity and selectivity.[19, 33, 52] To further confirm the synergy effect between adjacent Ni and Fe active sites in the Ni_7/Fe_3-N-C bimetallic catalysts toward CO_2 RR, a Ni_7/Fe_3-N-C-P sample was prepared by physical mixture of Ni-N-C and Fe-N-C with the same Ni/Fe ratio. In comparison to the Ni_7/Fe_3-N-C, the Ni_7/Fe_3-N-C-P sample showed a decreased FE(CO) at all applied potentials, demonstrating the important impact of neighbouring Ni and Fe active sites prepared by the chemical process towards CO_2 RR (Fig. S30). To further investigate the stability of the Ni_7/Fe_3-N-C during the CO_2 RR, a 30-h durability measurement is conducted, as shown in Fig. 4f. A CO_2 RR current density of around –5.6 mA cm^{-2} and a FE(CO) of over 90 % was maintained during the 30 h. All of the above results demonstrate that Ni_7/Fe_3-N-C has both a high catalytic activity and a high stability for CO_2 RR to CO. Finally, a 2-Ni_7/Fe_3-N-C sample was fabricated by using a two steps doping process, and investigated towards CO_2 RR, as shown in Fig. S31-S40. Notably, Ni_7/Fe_3-N-C and 2-Ni_7/Fe_3-N-C catalysts showed similar catalytic performances, demonstrating that our simple one-pot synthetic Ni and Fe co-doped IRMOF-3 could be directly used to prepare double metal active sites rather than the tedious multi-step doping process.

Theoretical Studies

Density Functional Theory (DFT) calculations were employed to further explore the origin of the improved CO_2 RR performance on the Ni_7/Fe_3-N-C sample. Based on the XAS results, a simulation model with neighbouring Ni and Fe sites embedded in N-doped graphene surface was created to represent the Ni_7/Fe_3-N-C catalyst. It is worth noting that there is an axial -OH ligand coordinated with the Fe atom. For comparison, the two single metal counterpart models for Ni-N-C and HO-Fe-N-C were also considered. We denote Ni sites in Ni-N-C catalyst as Ni-N-C-Ni, Fe sites in HO-Fe-N-C catalyst as HO-Fe-N-C-Fe, and Ni sites or Fe sites in Ni_7/Fe_3-N-C as Ni/Fe-N-C-Ni or Ni/Fe-N-C-Fe, respectively. The optimized structures and the optimal adsorption configurations of the reaction intermediates are shown in Fig. S41.

It is well established that there are three elementary steps during CO_2 RR, namely the formation of COOH*, conversion of COOH* to CO*, and the desorption of CO* from the active site, as shown in Fig. 5a.[19, 52, 53] The free energy profiles of CO_2 reduction to CO on different models at −0.5 V (vs. RHE) are illustrated in Fig. 5b. We can see that the free energy of COOH* formation on the Ni-N-C-Ni model is 0.83 eV, which is much higher than that of HO-Fe-N-C-Fe (−0.02 eV), which reflects the sluggish formation of COOH* on Ni sites. Regarding the CO* desorption process, it is exergonic on Ni-N-C-Ni due to the weak binding of CO* at the Ni active site. In contrast, it requires to overcome 0.47 eV of desorption free energy on HO-Fe-N-C-Fe due to the strong binding of CO* at the Fe site. These results reveal that the catalytic performances of single metal atom catalysts for CO_2 RR are limited by either the difficult formation of *COOH (on Ni sites) or the slow desorption of CO* (on Fe sites). When Ni and Fe were embedded adjacently in one catalyst model, a decrease of COOH* adsorption free energy could be seen over Ni/Fe-N-C-Ni (0.78 eV) compared to that over Ni-N-C-Ni (0.83 eV), while Ni/Fe-N-C-Fe (0.28 eV) exhibited a weaker COOH* adsorption free energy compared to HO-Fe-N-C-Fe (−0.02 eV). However, the presence of Ni sites could promote CO* desorption on Ni/Fe-N-C-Fe, and the desorption free energy is only 0.11 eV, which was much lower than that over HO-Fe-N-C-Fe (0.47 eV).

Meanwhile, the desorption of *CO over Ni/Fe-N-C-Ni was still spontaneous, which was similar to that for Ni-N-C-Ni. When comparing the reaction free energy of the most difficult step in CO_2 RR on HO-Fe-N-C-Fe (CO* desorption, 0.47 eV) and Ni/Fe-N-C-Fe (COOH* formation, 0.28 eV), we could find that the presence of Ni would promote the activity of CO_2 RR at Fe sites. Therefore, we found that this bimetallic catalyst showed a priority on CO_2 RR to CO due to its synergistic effect for *COOH formation and *CO desorption, leading to an excellent performance in CO_2 RR in comparison to the single metal counterparts. Taking into account all the above results, we suggest that Ni and Fe sites in this nano-reactor (Ni_7/Fe_3-N-C catalyst) could simultaneously adsorb COOH* and desorb CO*, but mainly influence different reaction steps, leading to an excellent performance in CO_2 RR.

Additionally, HER as a competing side reaction was also studied, and the free energy profiles obtained are shown in Fig. 5c. It can be found that Ni-N-C-Ni and Ni/Fe-N-C-Ni require relatively high free energies towards *H formation. In contrast, the adsorption free energies on HO-Fe-N-C-Fe and Ni/Fe-N-C-Fe are relatively lower (0.77 eV and 0.99 eV). These results suggest that HER occurs more easily on Fe sites than Ni sites, and that the existence of neighbouring Ni atoms can further hinder the HER on Fe atoms. Taking CO_2 RR and HER together into consideration, it can be concluded that the quasi-double-star Ni_7/Fe_3-N-C catalyst with adjacent Ni and Fe sites is superior for CO_2 RR, not only facilitating the formation of COOH* compared to the single Ni-N-C catalyst, and boosting the CO* desorption, but also limiting the undesired HER in comparison to the single Fe-N-C catalyst. These results are in good agreement with the experimental observations that Ni_7/Fe_3-N-C exhibits enhanced activity and selectivity for CO_2 RR over individual Ni-N-C and Fe-N-C catalysts.

Conclusions

In summary, we have demonstrated that a quasi-double-star catalyst composed of adjacent Ni and Fe active sites can enhance the activity towards CO_2 RR, in comparison to the single atom moieties. In this way, an atomically dispersed bimetallic Ni/Fe-N-C sample is successfully prepared through rationally controlling the Fe and Ni additive amounts into Zn-IRMOF-3, showing an excellent selectivity for generating CO (98 %) at a low overpotential (390 mV vs. RHE). These results are superior to those obtained in the single atom catalyst counterparts. Furthermore, the adjacent Ni and Fe active sites act as a nano-reactor, affecting different reaction steps in comparison to two separate active sites during CO_2 RR, thus, enhancing the overall activity. DFT simulations suggest that the adjacent Ni and Fe sites weaken the bonding energy of CO_2 RR intermediates as well as limit the competitive HER, and, thus, boost the CO_2 RR activity. Overall, this work provides a possibility for manipulating two active sites in a catalyst for improving both, selectivity and activity in CO_2 RR, simultaneously. The strategy employed here might be also adaptable for other electrocatalytic processes, such as, nitrogen reduction reaction (NRR), ORR and oxygen evolution reaction (OER).

Experimental section

Preparation of Ni-IRMOF-3, Fe-IRMOF-3, Ni_x/Fe_y-IRMOF-3

In this procedure, the fabrication process of M-IRMOF-3 is similar to the reported in literature with minor modification.[54] In detail, 932 mg $Zn(NO_3)_2 \cdot 6H_2O$ were dissolved in 100 ml DMF under magnetic stirring at room temperature to form a homogeneous solution. 181 mg 2-aminoterphthalic acid was added into the above mixture under ultrasonic for 5 min at room temperature. Then, 70 µl $Ni(NO_3)_2 \cdot 6H_2O$ or $FeCl_3 \cdot 6H_2O$ solution (10 mg ml^{-1}, DMF) were dropwise injected into the above solution under ultrasonic stirring until the formation of a clear solution. The obtained homogeneous solution was transferred into the Teflon-lined stainless-steel autoclave and reacted at 100 °C for 24 h. After cooling to room temperature, the powder was collected by centrifugation, washed with ethanol and DMF several times to remove organic residual. The final products denoted as Ni-IRMOF-3 or Fe-IRMOF-3 were then dried in vacuum at 65 °C overnight. Similarly, the Ni_x/Fe_y-IRMOF-3 were harvested by adding $Ni(NO_3)_2 \cdot 6H_2O$ (63 µl, 56 µl, 49 µl, 42 µl, 35 µl) and $FeCl_3 \cdot 6H_2O$ (7 µl, 14 µl, 21 µl, 28 µl, 35 µl) solution with different quantities. We denoted the resulting sample as Ni_x/Fe_y-IRMOF-3.

Preparation of 2-Ni_7/Fe_3-IRMOF-3

The 100 mg IRMOF-3 powder was dispersed in 10 ml DMF under ultrasound for 10 min at room temperature. After forming a homogeneous solution, $FeCl_3 \cdot 6H_2O$ (10 mg ml^{-1}, 9 µl) and $Ni(NO_3)_2 \cdot 6H_2O$ (10 mg ml^{-1}, 21 µl) solution were dropwise injected into the above solution under ultrasonic stirring for 5 min at room temperature. Next, the mixed solution was left under magnetic stirring at room temperature for 3 h. After reacting, the powder was collected by centrifugation, washed with ethanol and DMF several times to remove organic residual and dried in vacuum at 65 °C overnight. Then, we obtained the 2-Ni_7/Fe_3-IRMOF-3 sample.

Preparation of Ni-N-C, Fe-N-C, Ni_x/Fe_y-N-C and 2-Ni_7/Fe_3-N-C

As-prepared Ni-IRMOF-3 (or Fe-IRMOF-3, Ni_x/Fe_y-N-C and 2-Ni_7/Fe_3-N-C) powders were put in a porcelain boat. Subsequently, the samples were placed in a tube furnace and heated at 950 °C for 2 h with a heating rate of 5 °C min^{-1} under an Ar atmosphere to yield disperse Ni-N-C, Fe-N-C, Ni_x/Fe_y-N-C and 2-Ni_7/Fe_3-N-C.

Preparation of Physical Mixture Ni_7/Fe_3-N-C (Labelled as Ni_7/Fe_3-N-C)

For the preparation of the Ni_7/Fe_3-N-C-P sample, 3.5 mg of Ni-N-C powder were directly added into 1.5 mg of Fe-N-C powder. The powder was then mixed with a spoon.

Conflicts of interest

There are no conflicts to declare.

Acknowledgements

Authors acknowledge funding from Generalitat de Catalunya 2017 SGR 327 and 2017 SGR 1246. T.Z., J.R.M and J.A acknowledge funding from the Spanish MINECO project ENE2017-85087-C3. ICN2 is supported by the Severo Ochoa program from Spanish MINECO (Grant No. SEV-2017-0706). ICN2 and IREC are funded by the CERCA Programme / Generalitat de Catalunya. P.T acknowledges Humboldt Research Fellowship for Postdoctoral Researchers sponsored by the Alexander von Humboldt Foundation. X. Z acknowledges funding from FWO project (12ZV320N). Part of the present work has been performed in the framework of Universitat Autònoma de Barcelona Materials Science PhD program. T.Z and X.H thank China Scholarship Council for scholarship support (201706180028, 201804910551). The authors thank Guillaume Sauthier, Javier Saiz, Yunhui Yang for the XPS spectrum, FTIR, and ^{1}H-NMR tests.

Notes and references

1 J. Shen, R. Kortlever, R. Kas, Y. Y. Birdja, O. Diaz-Morales, Y. Kwon, I. Ledezma-Yanez, K. J. P. Schouten, G. Mul and M. T. M. Koper, *Nature Commun.*, 2015, **6**, 8177.

2 D. Gao, H. Zhou, F. Cai, J. Wang, G. Wang and X. Bao, *ACS Catal.*, 2018, **8**, 1510-1519.

3 J. Pei, T. Wang, R. Sui, X. Zhang, D. Zhou, F. Qin, X. Zhao, Q. Liu, W. Yan, J. Dong, L. Zheng, A. Li, J. Mao, W. Zhu, W. Chen and Z. Zhuang, *Energy Environ. Sci.*, 2021, DOI: 10.1039/D0EE03947K.

4 S. Gao, Y. Lin, X. Jiao, Y. Sun, Q. Luo, W. Zhang, D. Li, J. Yang and Y. Xie, *Nature*, 2016, **529**, 68-71.

5 Z. Chen, X. Zhang, W. Liu, M. Jiao, K. Mou, X. Zhang and L. Liu, *Energy Environ. Sci.*, 2021, DOI: 10.1039/D0EE04052E.

6 M. B. Gawande, P. Fornasiero and R. Zbořil, *ACS Catal.*, 2020, **10**, 2231-2259.

7 D. Zhao, Z. Zhuang, X. Cao, C. Zhang, Q. Peng, C. Chen and Y. Li, *Chem. Soc. Rev.*, 2020, **49**, 2215-2264.

8 Y. Yang, Y. Yang, Z. Pei, K.-H. Wu, C. Tan, H. Wang, L. Wei, A. Mahmood, C. Yan, J. Dong, S. Zhao and Y. Chen, *Matter*, 2020, **3**, 1442-1476.

9 A. Wang, J. Li and T. Zhang, *Nature Rev. Chem.*, 2018, **2**, 65-81.

10 D. Gao, T. Liu, G. Wang and X. Bao, *ACS Energy Lett.*, 2021, **6**, 713-727.

11 C. Zhao, X. Dai, T. Yao, W. Chen, X. Wang, J. Wang, J. Yang, S. Wei, Y. Wu and Y. Li, *J. Am. Chem. Soc.*, 2017, **139**, 8078-8081.

12 K. Jiang, S. Siahrostami, T. Zheng, Y. Hu, S. Hwang, E. Stavitski, Y. Peng, J. Dynes, M. Gangisetty, D. Su, K. Attenkofer and H. Wang, *Energy Environ. Sci.*, 2018, **11**, 893-903.

13 T. Zheng, K. Jiang, N. Ta, Y. Hu, J. Zeng, J. Liu and H. Wang, *Joule*, 2019, **3**, 265-278.

14 S. Liu, H. B. Yang, S.-F. Hung, J. Ding, W. Cai, L. Liu, J. Gao, X. Li, X. Ren, Z. Kuang, Y. Huang, T. Zhang and B. Liu, *Angew. Chem. Int. Ed.*, 2020, **59**, 798-803.

15 Y. Zhang, L. Jiao, W. Yang, C. Xie and H.-L. Jiang, *Angew. Chem. Int. Ed.*, 2021, **60**, 7607-7611.

16 C. F. Wen, F. Mao, Y. Liu, X. Y. Zhang, H. Q. Fu, L. R. Zheng, P. F. Liu and H. G. Yang, *ACS Catal.*, 2020, **10**, 1086-1093.

17 W. Xiong, H. Li, H. Wang, J. Yi, H. You, S. Zhang, Y. Hou, M. Cao, T. Zhang and R. Cao, *Small*, 2020, **16**, 2003943.

18 H. B. Yang, S.-F. Hung, S. Liu, K. Yuan, S. Miao, L. Zhang, X. Huang, H.-Y. Wang, W. Cai, R. Chen, J. Gao, X. Yang, W. Chen, Y. Huang, H. M. Chen, C. M. Li, T. Zhang and B. Liu, *Nature Energy*, 2018, **3**, 140-147.

19 W. Ren, X. Tan, W. Yang, C. Jia, S. Xu, K. Wang, S. C. Smith and C. Zhao, *Angew. Chem. Int. Ed.*, 2019, **58**, 6972-6976.

20 A. S. Varela, W. Ju, A. Bagger, P. Franco, J. Rossmeisl and P. Strasser, *ACS Catal.*, 2019, **9**, 7270-7284.

21 X.-M. Hu, H. H. Hval, E. T. Bjerglund, K. J. Dalgaard, M. R. Madsen, M.-M. Pohl, E. Welter, P. Lamagni, K. B. Buhl, M. Bremholm, M. Beller, S. U. Pedersen, T. Skrydstrup and K. Daasbjerg, *ACS Catal.*, 2018, **8**, 6255-6264.

22 O. S. Bushuyev, P. De Luna, C. T. Dinh, L. Tao, G. Saur, J. van de Lagemaat, S. O. Kelley and E. H. Sargent, *Joule*, 2018, **2**, 825-832.

23 L. Cao, D. Raciti, C. Li, K. J. T. Livi, P. F. Rottmann, K. J. Hemker, T. Mueller and C. Wang, *ACS Catal.*, 2017, **7**, 8578-8587.

24 C. Ding, A. Li, S.-M. Lu, H. Zhang and C. Li, *ACS Catal.*, 2016, **6**, 6438-6443.

25 X. Wang, J. F. de Araújo, W. Ju, A. Bagger, H. Schmies, S. Kühl, J. Rossmeisl and P. Strasser, *Nature Nanotechnol.*, 2019, **14**, 1063-1070.

26 L. Lin, T. Liu, J. Xiao, H. Li, P. Wei, D. Gao, B. Nan, R. Si, G. Wang and X. Bao, *Angew. Chem. Int. Ed.*, 2020, **59**, 22408-22413.

27 D. Gao, R. M. Arán-Ais, H. S. Jeon and B. Roldan Cuenya, *Nature Catal.*, 2019, **2**, 198-210.

28 L. Bai, C.-S. Hsu, D. T. L. Alexander, H. M. Chen and X. Hu, *J. Am. Chem. Soc.*, 2019, **141**, 14190-14199.

29 Y. Cheng, S. He, J.-P. Veder, R. De Marco, S.-z. Yang and S. Ping Jiang, *ChemElectroChem*, 2019, **6**, 3478-3487.

30 S. Wang, L. Shi, X. Bai, Q. Li, C. Ling and J. Wang, *ACS Cent. Sci.*, 2020, **6**, 1762-1771.

31 J. Wang, Z. Huang, W. Liu, C. Chang, H. Tang, Z. Li, W. Chen, C. Jia, T. Yao, S. Wei, Y. Wu and Y. Li, *J. Am. Chem. Soc.*, 2017, **139**, 17281-17284.

32 S. Sarkar, A. Biswas, T. Purkait, M. Das, N. Kamboj and R. S. Dey, *Inor. Chem.*, 2020, **59**, 5194-5205.

33 Y. Zhou, W. Yang, W. Utetiwabo, Y.-m. Lian, X. Yin, L. Zhou, P. Yu, R. Chen and S. Sun, *J. Phys. Chem. Lett.*, 2020, **11**, 1404-1410.

34 Y. Luan, Y. Qi, H. Gao, R. S. Andriamitantsoa, N. Zheng and G. Wang, *J. Mater. Chem. A*, 2015, **3**, 17320-17331.

35 L. Ye, Y. Ying, D. Sun, Z. Zhang, L. Fei, Z. Wen, J. Qiao and H. Huang, *Angew. Chem. Int. Ed.*, 2020, **59**, 3244-3251.

36 H. Yang, Y. Wu, G. Li, Q. Lin, Q. Hu, Q. Zhang, J. Liu and C. He, *J. Am. Chem. Soc.*, 2019, **141**, 12717-12723.

37 Q. Zhang, H. Jiang, D. Niu, X. Zhang, S. Sun and S. Hu, *ChemistrySelect*, 2019, **4**, 4398-4406.

38 S. Liu, H. Yang, X. Huang, L. Liu, W. Cai, J. Gao, X. Li, T. Zhang, Y. Huang and B. Liu, *Adv. Func. Mater.*, 2018, **28**, 1800499.

39 C. Zhao, Y. Wang, Z. Li, W. Chen, Q. Xu, D. He, D. Xi, Q. Zhang, T. Yuan, Y. Qu, J. Yang, F. Zhou, Z. Yang, X. Wang, J. Wang, J. Luo, Y. Li, H. Duan, Y. Wu and Y. Li, *Joule*, 2019, **3**, 584-594.

40 D. Guo, R. Shibuya, C. Akiba, S. Saji, T. Kondo and J. Nakamura, *Science*, 2016, **351**, 361-365.

41 L. Gong, H. Zhang, Y. Wang, E. Luo, K. Li, L. Gao, Y. Wang, Z. Wu, Z. Jin, J. Ge, Z. Jiang, C. Liu and W. Xing, *Angew. Chem. Int. Ed.*, 2020, **59**, 13923-13928.

42 T. Yamamoto, *X-Ray Spectrom.*, 2008, **37**, 572-584.

43 H. Zhang, J. Li, S. Xi, Y. Du, X. Hai, J. Wang, H. Xu, G. Wu, J. Zhang, J. Lu and J. Wang, *Angew. Chem. Int. Ed.*, 2019, **58**, 14871-14876.

44 S. Zhao, L. Zhang, B. Johannessen, M. Saunders, C. Liu, S.-Z. Yang and S. P. Jiang, *Adv. Mater. Interfaces*, 2021, **8**, 2001788.

45 J. Li, P. Pršlja, T. Shinagawa, A. J. Martín Fernández, F. Krumeich, K. Artyushkova, P. Atanassov, A. Zitolo, Y. Zhou, R. García-Muelas, N. López, J. Pérez-Ramírez and F. Jaouen, *ACS Catal.*, 2019, **9**, 10426-10439.
46 Y. Chen, S. Ji, Y. Wang, J. Dong, W. Chen, Z. Li, R. Shen, L. Zheng, Z. Zhuang, D. Wang and Y. Li, *Angew.e Chem. Int. Ed.*, 2017, **56**, 6937-6941.
47 Z. Chen, A. Huang, K. Yu, T. Cui, Z. Zhuang, S. Liu, J. Li, R. Tu, K. Sun, X. Tan, J. Zhang, D. Liu, Y. Zhang, P. Jiang, Y. Pan, C. Chen, Q. Peng and Y. Li, *Energy Environ. Sci.*, 2021, DOI: 10.1039/D1EE00569C.
48 L. Xia, H. Song, X. Li, X. Zhang, B. Gao, Y. Zheng, K. Huo and P. K. Chu, *Front. Chem.*, 2020, **8**.
49 T. Zhang, J. Du, P. Xi and C. Xu, *ACS Appl. Mater. Interfaces*, 2017, **9**, 362-370.
50 J. Gu, C.-S. Hsu, L. Bai, H. M. Chen and X. Hu, *Science*, 2019, **364**, 1091-1094.
51 T. Li, C. Yang, J.-L. Luo and G. Zheng, *ACS Catal.*, 2019, **9**, 10440-10447.
52 W. Zhu, L. Zhang, S. Liu, A. Li, X. Yuan, C. Hu, G. Zhang, W. Deng, K. Zang, J. Luo, Y. Zhu, M. Gu, Z.-J. Zhao and J. Gong, *Angew. Chem. Int. Ed.*, 2020, **59**, 12664-12668.
53 P. P. Sharma, J. Wu, R. M. Yadav, M. Liu, C. J. Wright, C. S. Tiwary, B. I. Yakobson, J. Lou, P. M. Ajayan and X.-D. Zhou, *Angew. Chem. Int. Ed.*, 2015, **54**, 13701-13705.
54 S. J. Lyle, R. W. Flaig, K. E. Cordova and O. M. Yaghi, *J. Chem. Edu.*, 2018, **95**, 1512-1519.

SUPPORTING INFORMATION

Quasi-Double-Star Nickel and Iron Active Sites for High-Efficient Carbon Dioxide Electroreduction

Ting Zhang,[a,b] Xu Han,[a] Hong Liu,[c] Martí Biset-Peiró,[b] Xuan Zhang,[d,e] Pingping Tan,[e] Pengyi Tang,*[f,g] Bo Yang,[c] Lirong Zheng,*[h] Joan Ramon Morante,[b,i] Jordi Arbiol*[a,j]

[a]Catalan Institute of Nanoscience and Nanotechnology (ICN2), CSIC and BIST, Campus UAB, Bellaterra, Barcelona, 08193, Catalonia, Spain

[b]Catalonia Institute for Energy Research (IREC), Jardins de les Dones de Negre 1, Sant Adrià del Besòs, Barcelona, 08930, Catalonia, Spain

[c]School of Physical Science and Technology, ShanghaiTech University, 393 Middle Huaxia Road, Shanghai, 201210, P. R. China

[d]Department of Materials Engineering, KU Leuven, Kasteelpark Arenberg, 44, B-3001 Leuven, Belgium

[e]Institute for Clean Energy & Advanced Materials, Faculty of Materials & Energy, Southwest University, Chongqing 400715, China.

[f]Ernst Ruska-Centre for Microscopy and Spectroscopy with Electrons and Peter Grünberg Institute, Forschungszentrum Jülich GmbH, Jülich, 52425, Germany

[g]Institute of Microsystem and Information Technology, Chinese Academy of Sciences, Shanghai, 200050, P. R. China

[h]Beijing Synchrotron Radiation Facility, Institute of High Energy Physics, Chinese Academy of Sciences, Beijing, 100049, P. R. China

[i]Department of Physics, Universitat de Barcelona, Barcelona, 08028, Catalonia, Spain

[j]ICREA, Pg. Lluís Companys 23, Barcelona, 08010, Catalonia, Spain

*Correspondence: py.tang@mail.sim.ac.cn (P.T)

*Correspondence: zhenglr@ihep.ac.cn (L.Z)

*Correspondence: arbiol@icrea.cat (J.A)

CONTENTS

Materials and Methods

Materials:

If not specified, all chemical reagents were purchased from Sigma-Aldrich. Zinc nitrate hexahydrate ($Zn(NO_3)_2 \cdot 6H_2O$), 2-Aminoterphthalic acid, iron chloride hexahydrate ($FeCl_3 \cdot 6H_2O$), cobaltous nitrate hexahydrate ($Co(NO_3)_2 \cdot 6H_2O$), nickel chloride hexahydrate ($NiCl_2 \cdot 6H_2O$), N,N-dimethylformamide (DMF), sodium thiocyanate (NaSCN), ethanol and sodium bicarbonate ($NaHCO_3$) were all of analytical grade and used as received without further purification. Meanwhile, all solutions were prepared with Milli-Q water (DI-H_2O, Ricca Chemical, ASTM Type I). The carbon paper was purchased from Alfa Aesar. The Nafion (N-117 membrane, 0.18 mm thick) was also purchased from Alfa Aesar and kept in 0.5 M NaOH solution.

Characterization:

The X-ray diffraction patterns (XRD) were obtained through a Bruker D4 X-ray powder diffractometer using Cu Kα radiation (1.54184 Å). Field emission scanning electron microscopy (FESEM) images were collected on a FEI Magellan 400 L scanning electron microscope. The transmission electron microscopy (TEM) and high angle annular dark field scanning TEM (HAADF STEM) images were obtained in a Tecnai F20 field emission gun microscope with a 0.19 nm point-to-point resolution at 200 kV equipped with an embedded Quantum Gatan Image Filter for EELS analyses. Images have been analyzed by means of Gatan Digital Micrograph software. Parts of HAADF-STEM images and elemental mapping (EDX) were obtained in a spherical aberration-corrected (AC) transmission electron microscope FEI Themis Z and operated at 200 kV. X-ray photoelectron spectroscopy (XPS) was performed on a Phoibos 150 analyser (SPECS GmbH, Berlin, Germany) in ultra-high vacuum conditions (base pressure 4×10^{-10} mbar) with a monochromatic aluminum Kα X-ray source (1486.74 eV). Binding energies (BE) were determined using the C 1s peak at 284.5 eV as a charge reference. Inductively coupled plasma-mass spectrometry (ICP-MS) measurements were carried out to determine the concentration of Fe. Brunauer-Emmett-Teller (BET) surface areas were measured using nitrogen adsorption at 77 K. Raman spectra were obtained using Senterra. Fourier transformed infrared (FTIR) spectroscopy data were recorded on an Alpha Bruker spectrometer. Thermogravimetric Analysis was measured by Pyris 1 TGA, Perkin Elmer.

XAFS Measurements:

The X-ray absorption find structure spectra (Fe K-edge) were collected at 1W1B station in Beijing Synchrotron Radiation Facility (BSRF). The storage rings of BSRF were operated at 2.5 GeV with an average current of 250 mA. Using Si(111) double-crystal monochromator, the data collection were carried out in transmission/fluorescence mode using ionization chamber. All spectra were collected in ambient conditions.

XAFS Analysis and Results:

The acquired EXAFS data were processed according to the standard procedures using the ATHENA module implemented in the IFEFFIT software packages. The k^3-weighted EXAFS spectra were obtained by subtracting the post-edge background from the overall absorption and then normalizing with respect to the edge-jump step. Subsequently, k^3-weighted $\chi(k)$ data of Fe K-edge were Fourier transformed to real (R) space using a hanning windows (dk=1.0 Å^{-1}) to separate the EXAFS contributions from different coordination shells. To obtain the quantitative structural parameters around central atoms, least-squares curve parameter fitting was performed using the ARTEMIS module of IFEFFIT software packages.[1-3]

Ink Preparation:

2 mg synthesized different samples and 50 μl 5 wt% Nafion solutions were dissolved in ethanol (1 ml) and ultrasonicated for 1 h to form evenly suspension for the further electrochemical experiments. To prepare the working electrode, 500 μL above as-prepared inks were dropped onto the two sides of the carbon paper electrode with 1×1 cm^2 and then dried at room temperature for a few minutes, giving a catalyst loading mass of ~1 mg cm^{-2}.

Electrochemical Measurement:

The electrocatalytic performance of different catalysts was measured at room temperature by using a gas-tight H-cell with two-compartments separated by a cation exchange membrane (Nafion N-117 membrane) with a continuously Ar or CO_2 gas injection. Each compartment contained 70 ml electrolyte (0.5 M $NaHCO_3$ made from de-ionized water). In a typical experiment, a standard three electrode setup in 0.5 M $NaHCO_3$ solution was assembled: an Ag/AgCl electrode as a reference electrode, a Pt plate as a counter electrode and a carbon paper coated with the different samples as a working electrode (surface area = 1 cm^2). The potentials were measured versus Ag/AgCl and converted to the reversible hydrogen electrode (RHE) according to the following equation: $E_{RHE} = E^0_{Ag/AgCl} + E_{Ag/AgCl} + 0.059 \times pH$, pH=7.[4] All electrochemical results were showed without iR-compensation by using a computer-controlled BioLogic VMP3 electrochemical workstation. Meanwhile, the linear sweep voltammetry (LSV) was performed at a scan rate of 20 mV s^{-1} from 0 V to −1.5 V vs. Ag/AgCl in Ar-saturated 0.5 M $NaHCO_3$ (pH=8.5) and CO_2-saturated 0.5 M $NaHCO_3$ (pH=7) as supporting electrolyte. The cyclic voltammetry (CV) was performed at a scan rate of 20 mV s^{-1}. Moreover, electrochemical impedance spectroscopy (EIS) of different samples was carried out in a frequency range from 100 kHz to 100 mHz.

Before the electrochemical CO_2 reduction experiments, an average rate of 20 ml min^{-1} Ar was injected into cathodic electrolyte in order to form an Ar-saturated solution. During electrochemical CO_2 reduction experiments, the CO_2 gas was delivered at an average rate of 20 ml min^{-1} at room temperature and ambient pressure, measured downstream by a volumetric digital flowmeter. The gas phase composition was analyzed by gas chromatography (GC) during potentiostatic measurements every 20 min. The calibration of peak area vs. gas concentration was used for the molar quantification of each gaseous effluent. The Faradaic efficiency was calculated by determining the number of coulombs needed for each product and then dividing by the total charge passed during the time of the GC sampling according to the flow rate. Liquid products were analyzed afterwards by quantitative ^{1}H-NMR using water as the deuterated solvent.

Calculation Method:

Details concerning the Faradaic Efficiency (FE) calculations are shown below.[4-6]

The partial current density for a given gas product was calculated as below:

$$j_i = x_i \times V \times \frac{n_i F P_0}{RT} \times (electrode\ area)^{-1}$$

Where x_i is the volume fraction of a certain product determined by online GC referenced to calibration curves from three standard gas samples, V is the flow rate, n_i is the number of electrons involved, P_0= 101.3 kPa, F is the Faraday constant, and R is the gas constant. The corresponding FE at each potential is calculated by

$$FE = \frac{j_i}{j} \times 100\%$$

DFT Calculations:

The spin-polarized DFT calculations with projector augmented wave (PAW) method[7-10] were performed using the Vienna ab initio Simulation Package (VASP) code.[11] The Bayesian error estimation functional with van der Waals correlation (BEEF-vdW) was employed to set the plane wave basis.[12] The convergence criteria were 0.05 eV/ Å in force and 1×10^{-4} eV in energy and the plane wave cutoff was 500 eV. The Monkhorst–Pack mesh k-point grids were 2×2×1 for all models. All the vacuum thicknesses were higher than 15 Å. With the BEEF-vdW function, the energy of the gas phase molecules gave a systematic correction by +0.41 and +0.09 eV for gaseous CO_2 and H_2, respectively.[13-15] For the electroreduction of CO_2 to CO, the following elementary steps were considered:

$$CO_2(g) + * + H^+(aq) + e^- \leftrightarrow COOH* \qquad \text{(Equation S.1)}$$

$$COOH* + H^+(aq) + e^- \leftrightarrow CO* + H_2O(l) \qquad \text{(Equation S.2)}$$

$$CO* \leftrightarrow CO(g) + * \qquad \text{(Equation S.3)}$$

where (g), (aq) represent the gaseous phase and aqueous phase, respectively. The *, COOH* and CO* represent free site, adsorption state of COOH and CO, respectively. The reaction free energies of each step was calculated by the following formula:

$$G = E_{\mathrm{DFT}} + E_{\mathrm{ZPE}} + \int C_p \mathrm{d}T - TS + E_{\mathrm{sol}} \qquad \text{(Equation S.4)}$$

the E_{DFT} is the DFT calculated energy, E_{ZPE} is the zero-point energy, C_p is the constant pressure heat capacity, T is temperture, S is the entropy. The E_{sol} is solvation correction, which is -0.1 eV for CO* and -0.25 eV COOH*.[16] The temperature for the reaction is considered as 298.15 K here.

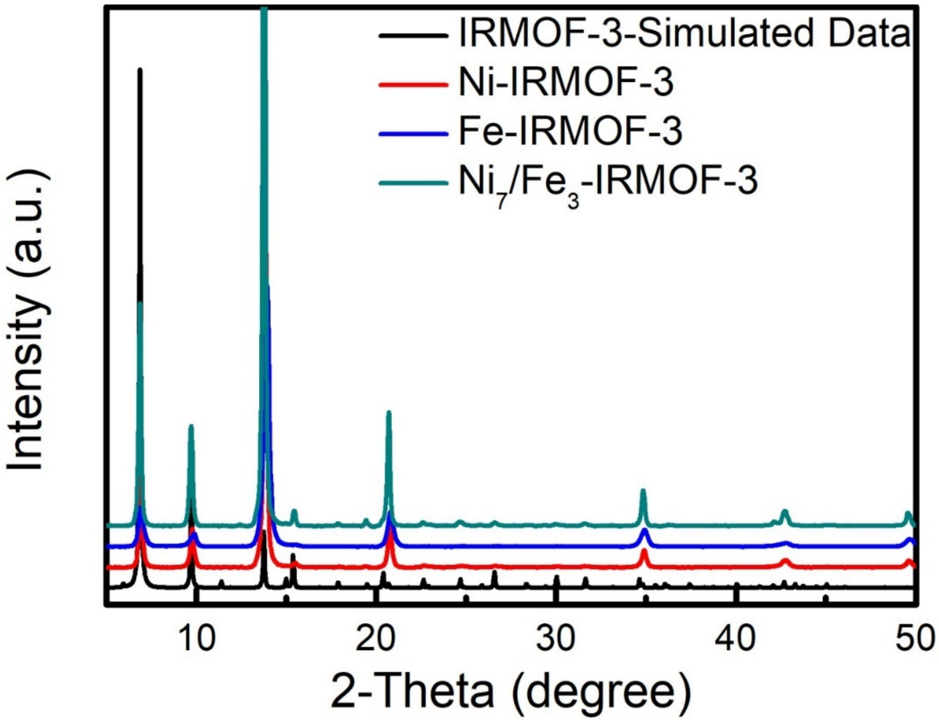

Fig. S1. XRD patterns of Ni-IRMOF-3, Fe-IRMOF-3 and Ni_7/Fe_3-IRMOF-3.

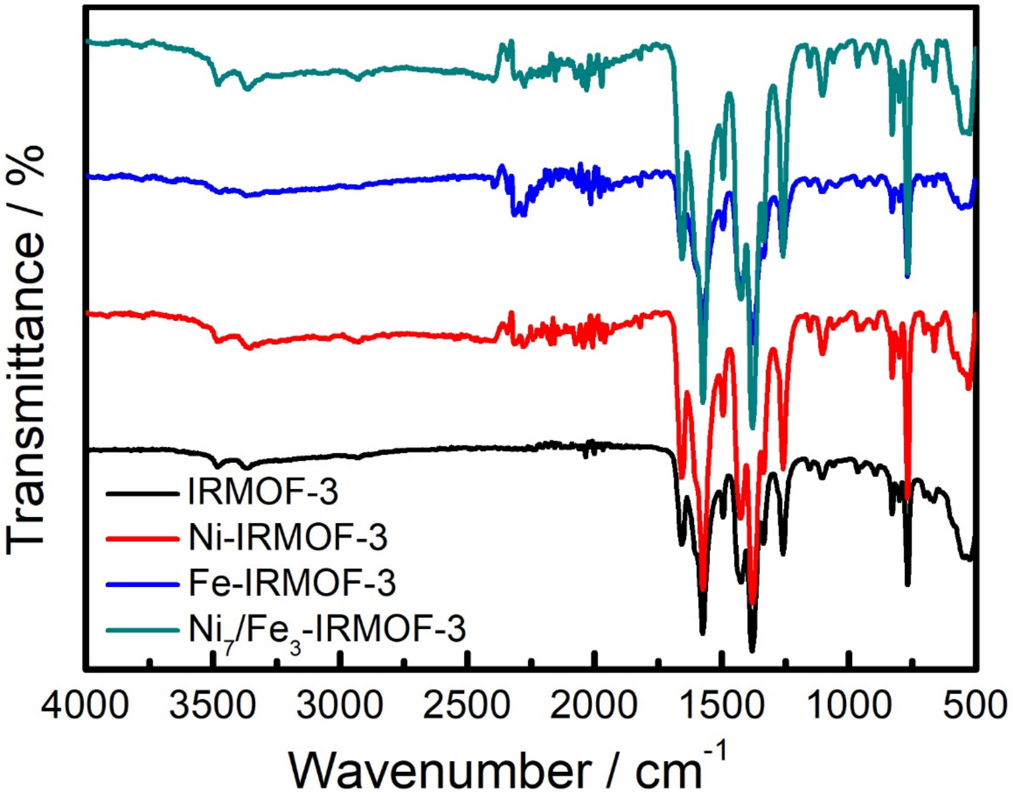

Fig. S2. FTIR spectrum of IRMOF-3, Ni-IRMOF-3, Fe-IRMOF-3 and Ni_7/Fe_3-IRMOF-3.

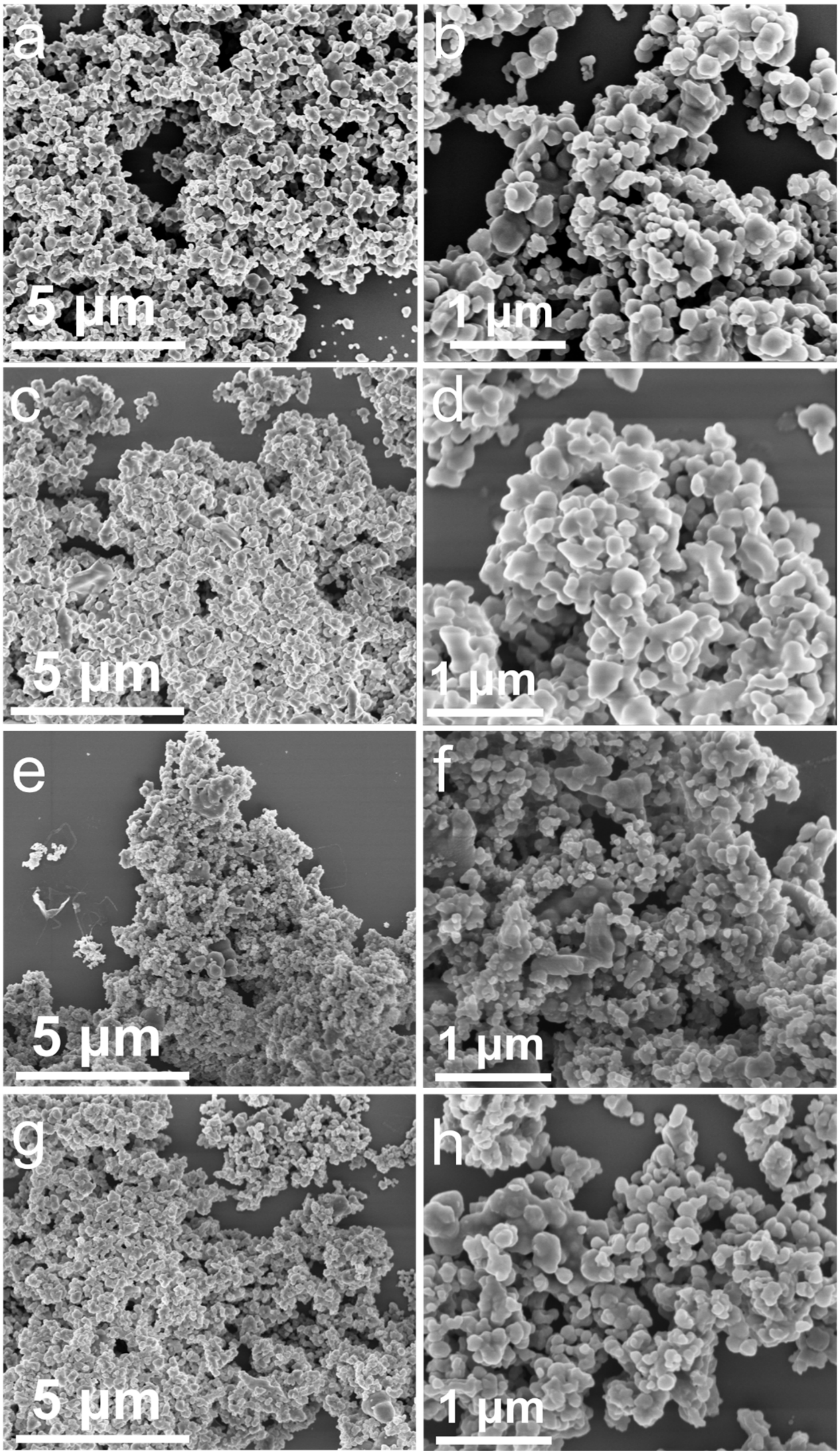

Fig. S3. SEM images of (a and b) IRMOF-3, (c and d) Ni-IRMOF-3, (e and f) Fe-IRMOF-3, (g and h) Ni_7/Fe_3-IRMOF-3.

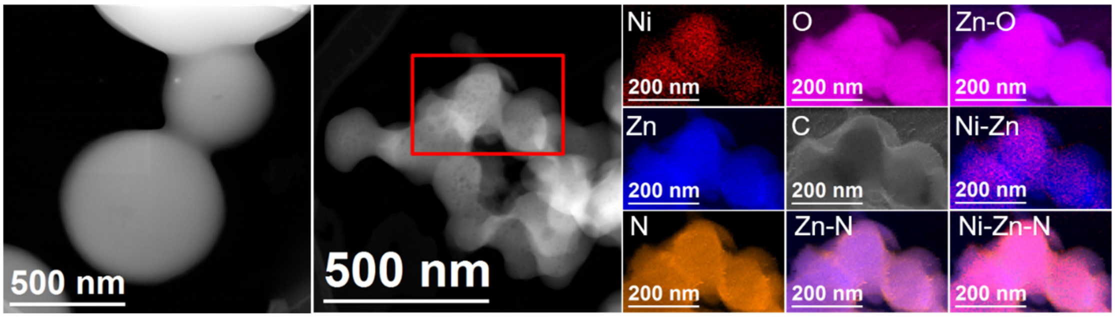

Fig. S4. HAADF STEM image of Ni-IRMOF-3 and representative EELS chemical composition maps obtained from the red squared area of the STEM micrograph. Individual Ni $L_{2,3}$-edges at 855 eV (red), Zn $L_{2,3}$-edges at 1020 eV (blue), N K-edges at 401 eV (orange), O K-edges at 532 eV (pink) and C K-edges at 285 eV (grey) as well as composites of Zn-N, Zn-O, Ni-Zn and Ni-Zn-N.

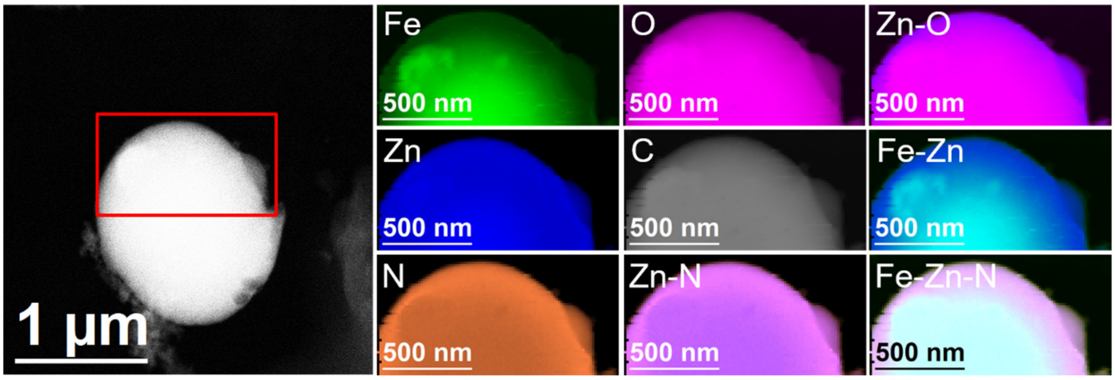

Fig. S5. HAADF STEM image of Fe-IRMOF-3 and representative EELS chemical composition maps obtained from the red squared area of the STEM micrograph. Individual Fe $L_{2,3}$-edges at 708 eV (green), Zn $L_{2,3}$-edges at 1020 eV (blue), N K-edges at 401 eV (orange), O K-edges at 532 eV (pink) and C K-edges at 285 eV (grey) as well as composites of Zn-N, Zn-O, Fe-Zn and Fe-Zn-N.

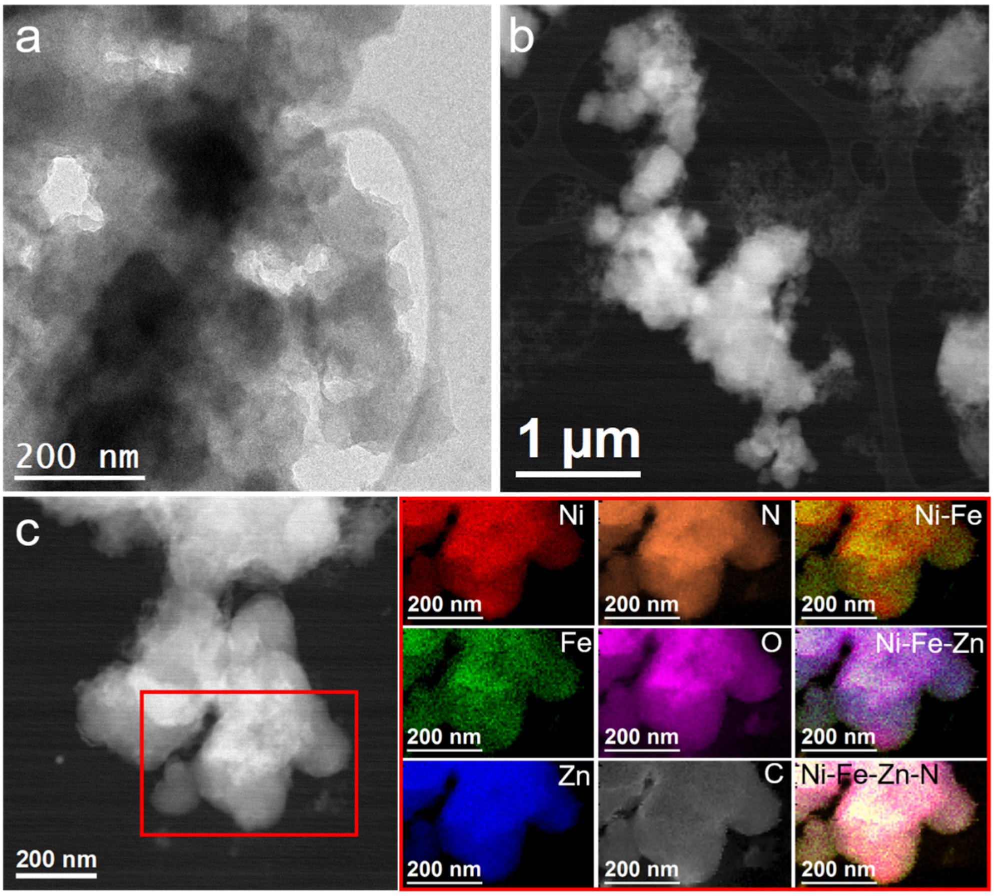

Fig. S6. (a) BF TEM, (b, c) HAADF STEM image of Ni$_7$/Fe$_3$-IRMOF-3 and representative EELS chemical composition maps obtained from the red squared area of the STEM micrograph. Individual Ni L$_{2,3}$-edges at 855 eV (red), Fe L$_{2,3}$-edges at 708 eV (green), Zn L$_{2,3}$-edges at 1020 eV (blue), N K-edges at 401 eV (orange), O K-edges at 532 eV (pink) and C K-edges at 285 eV (grey) as well as composites of Ni-Fe, Ni-Fe-Zn and Ni-Fe-Zn-N.

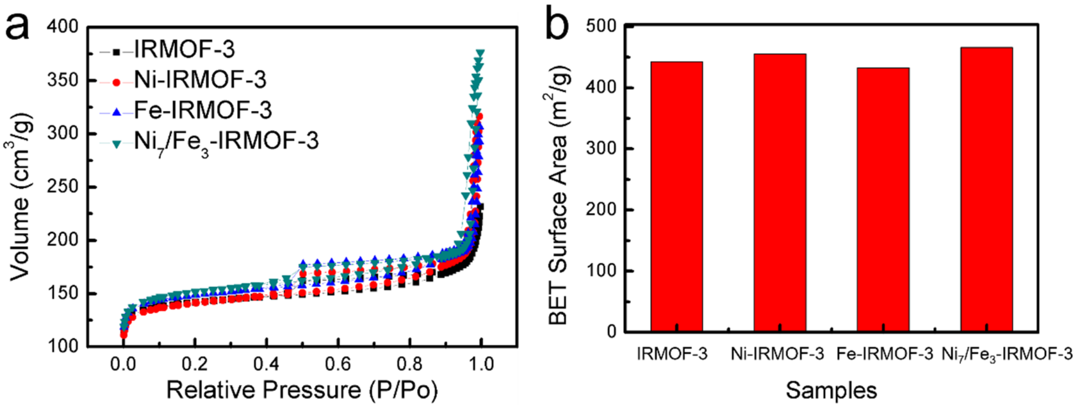

Fig. S7. (a) N_2 adsorption and desorption isotherm and (b) BET surface areas for IRMOF-3, Ni-IRMOF-3, Fe-IRMOF-3 and Ni_7/Fe_3-IRMOF-3.

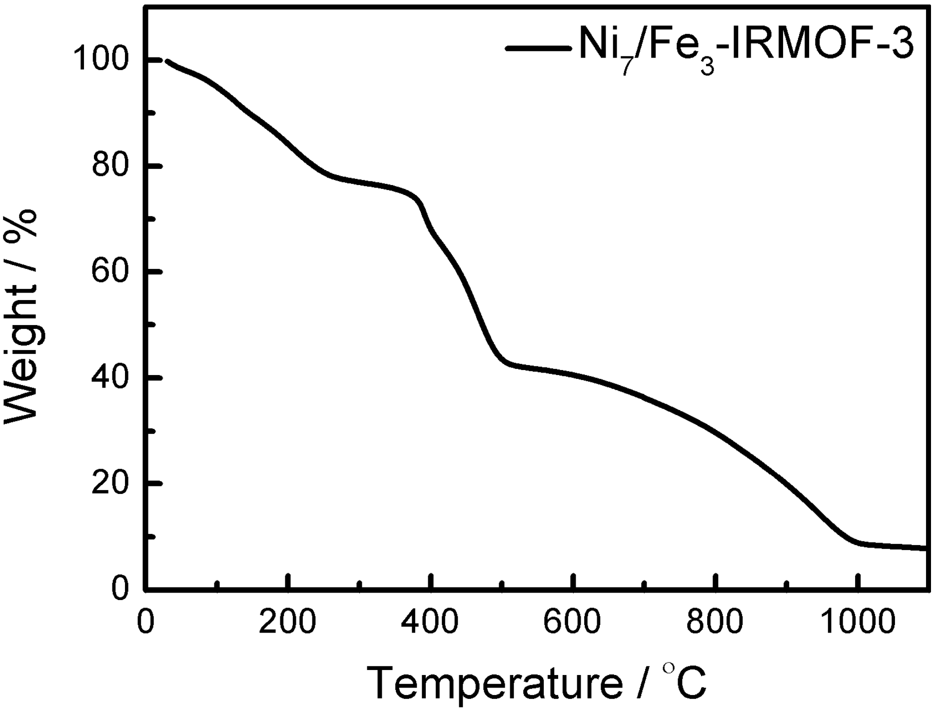

Fig. S8. TGA patterns of Ni_7/Fe_3-IRMOF-3.

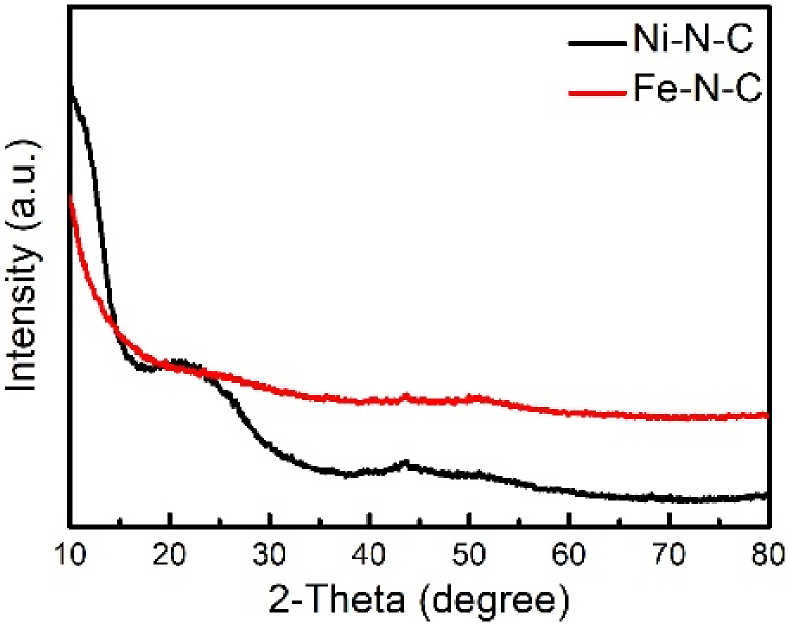

Fig. S9. XRD patterns of Ni-N-C and Fe-N-C.

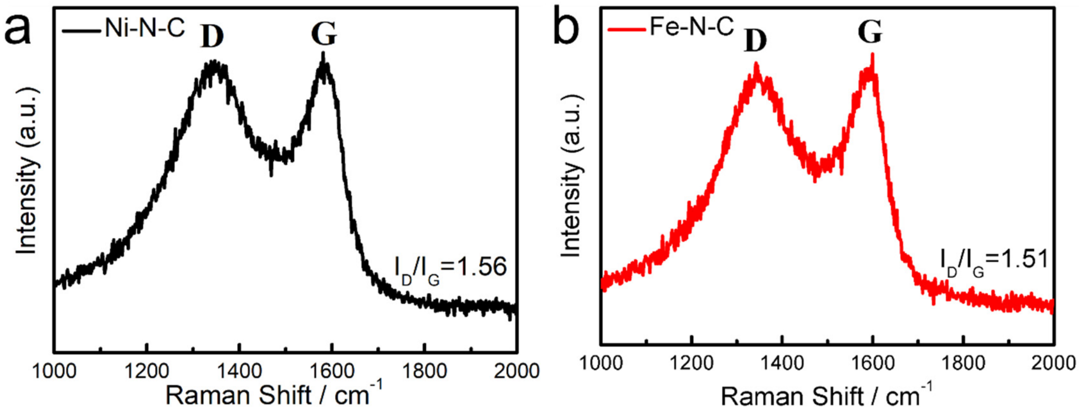

Fig. S10. Raman spectra of (a) Ni-N-C and (b) Fe-N-C.

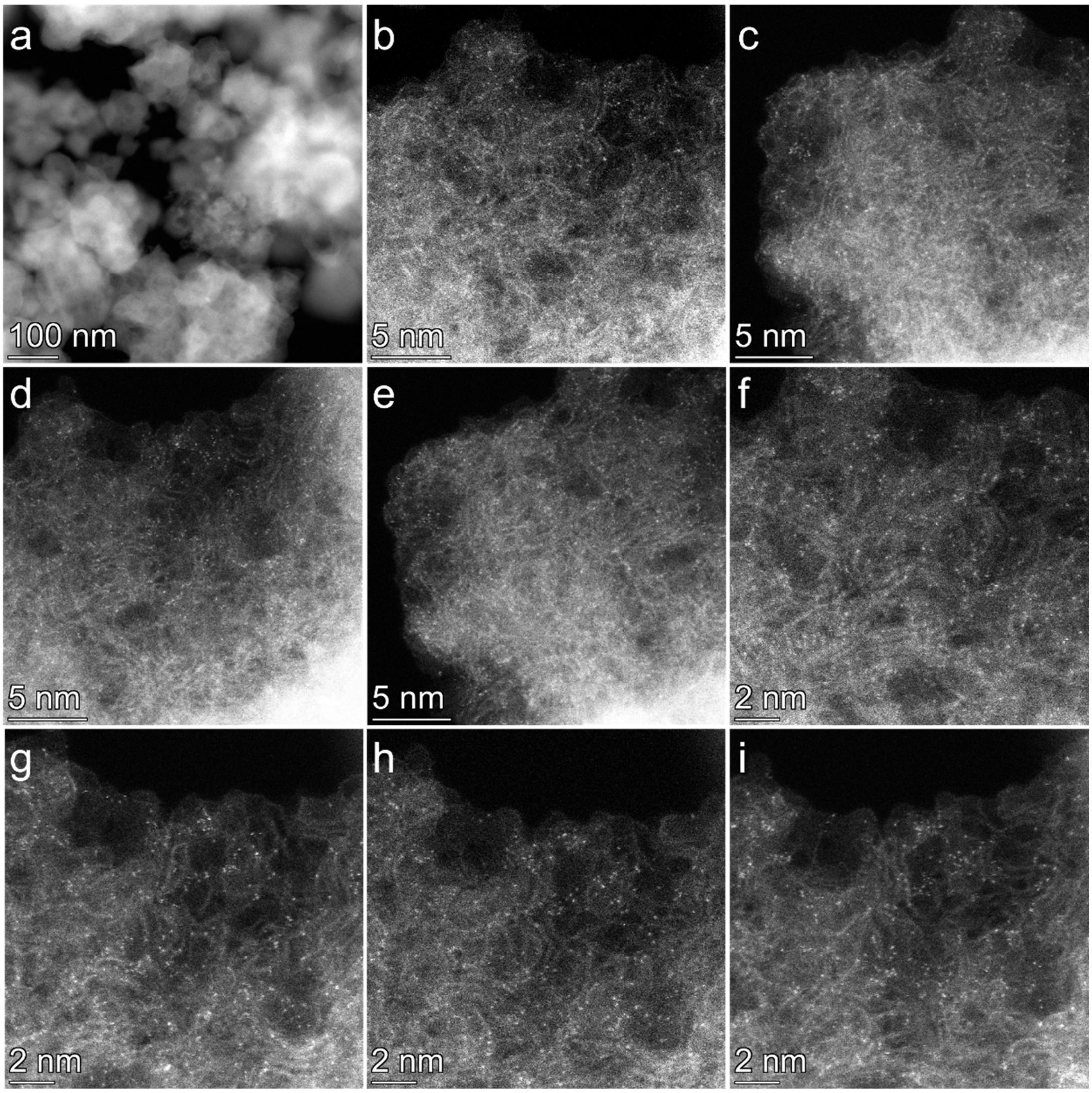

Fig. S11. (a) Low magnification and (b-i) high magnification aberration-corrected HAADF STEM images of Ni_7/Fe_3-N-C sample.

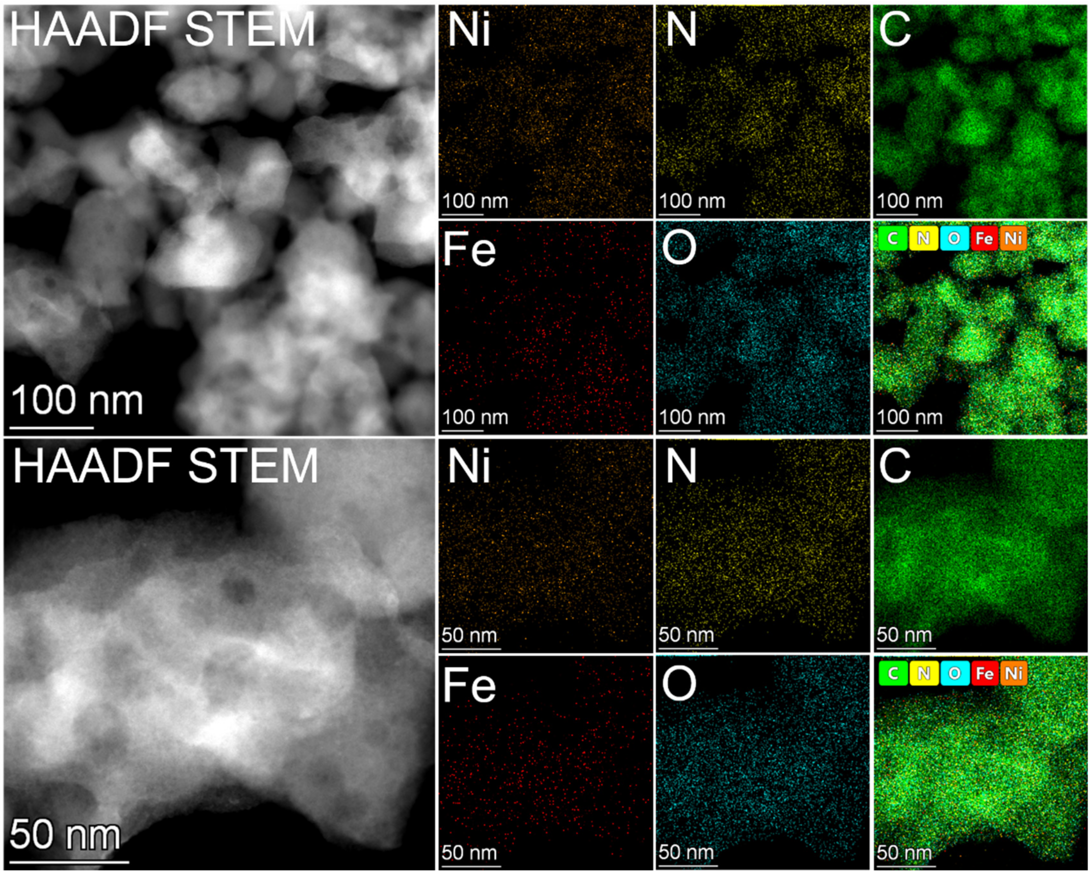

Fig. S12. HAADF STEM image of Ni_7/Fe_3-N-C and representative EDX chemical composition maps.

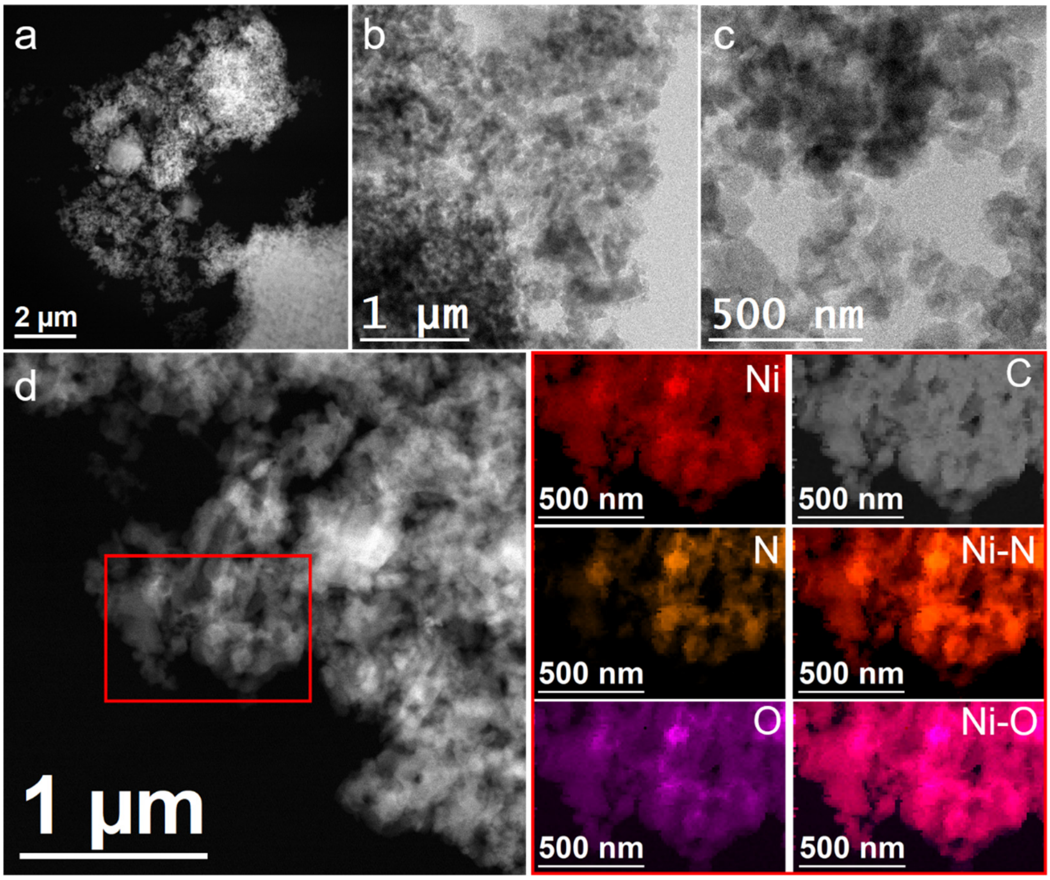

Fig. S13. (a) HAADF STEM, (b, c) BF TEM images of Ni-N-C, (d) HAADF STEM image and representative EELS chemical composition maps obtained from the red squared area of the STEM micrograph. Individual Ni $L_{2,3}$-edges at 855 eV (red), N K-edges at 401 eV (orange), O K-edges at 532 eV (pink) and C K-edges at 285 eV (grey) as well as composites of Ni-N and Ni-O.

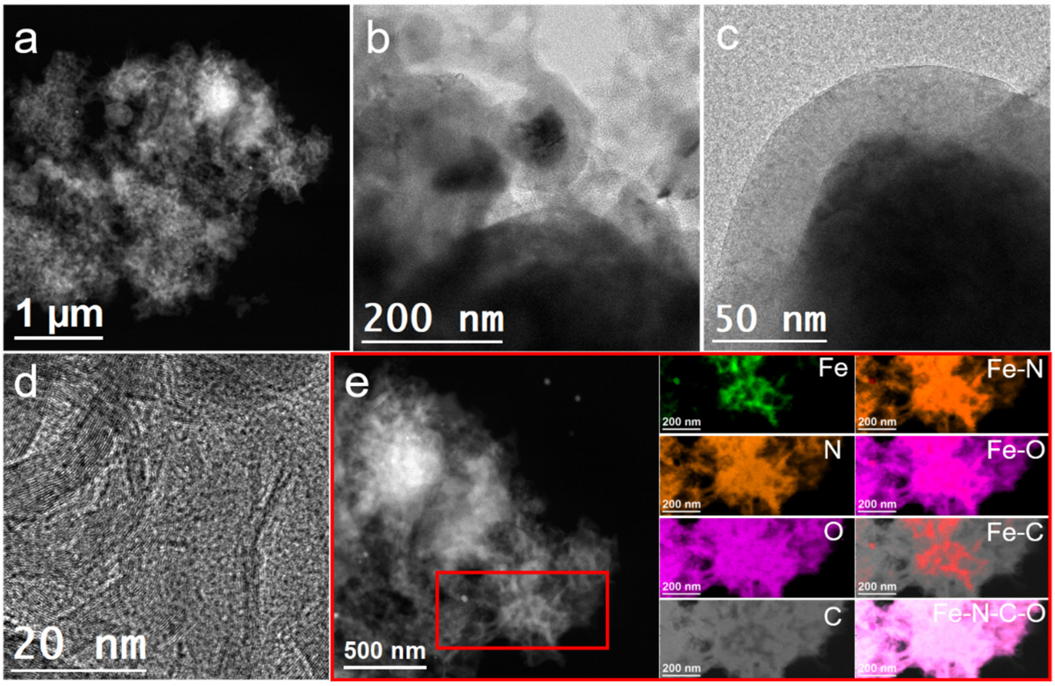

Fig. S14. (a) HAADF STEM, (b, c) BF TEM, (d) HRTEM images of Fe-N-C as well as (e) HAADF STEM image and representative EELS chemical composition maps obtained from the red squared area of the STEM micrograph. Individual Fe $L_{2,3}$-edges at 708 eV (green), N K-edges at 401 eV (orange), O K-edges at 532 eV (pink) and C K-edges at 285 eV (grey) as well as composites of Fe-N, Fe-O, Fe-C and Fe-N-C-O.

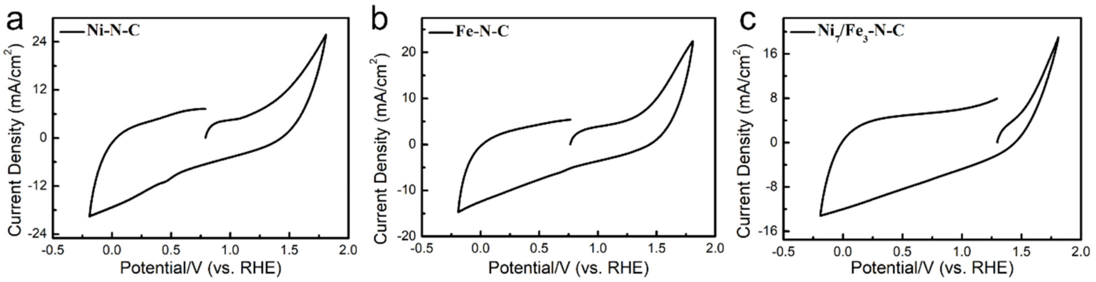

Fig. S15. CV curves of (a) Ni-N-C, (b) Fe-N-C and (c) Ni_7/Fe_3-N-C in 0.5 M $NaHCO_3$ electrolyte.

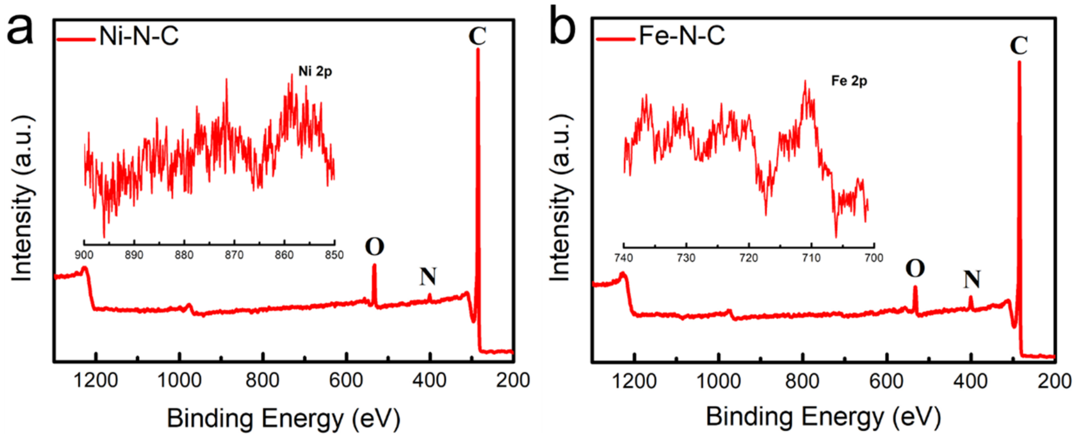

Fig. S16. XPS survey spectra of (a) Ni-N-C (inset) Ni 2p and (b) Fe-N-C (inset) Fe 2p.

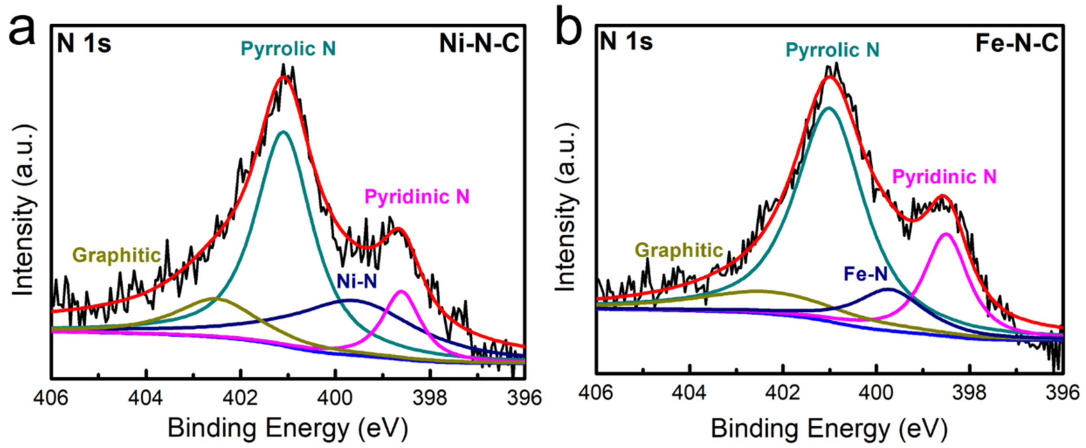

Fig. S17. High-resolution XPS N 1s of (a) Ni-N-C and (b) Fe-N-C.

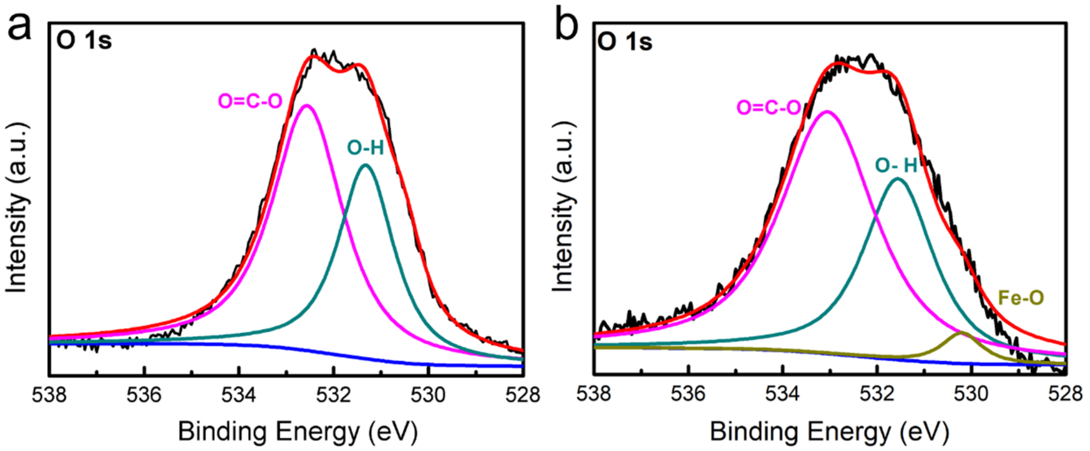

Fig. S18. High-resolution XPS O 1s of (a) Ni-N-C and (b) Fe-N-C.

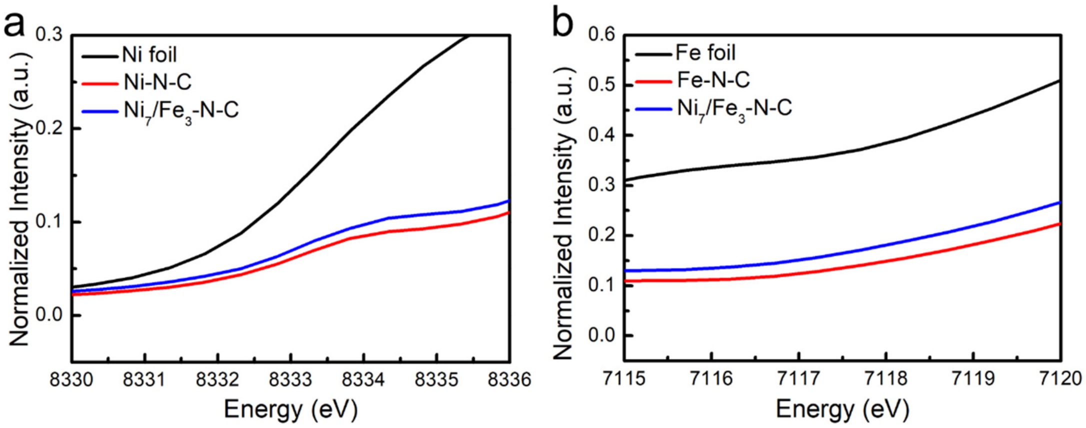

Fig. S19. The enlarged pre-edge region of (a) Ni K-edge XANES spectra and (b) Fe K-edge XANES spectra.

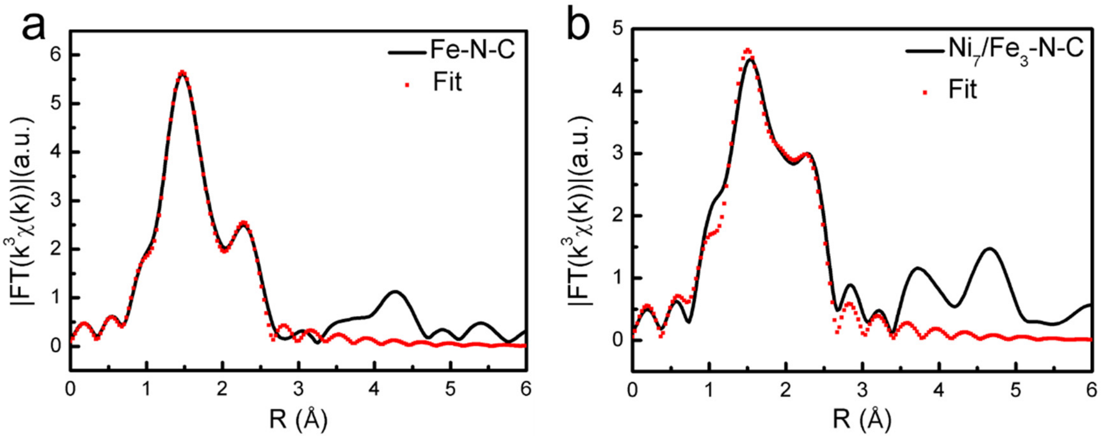

Figure S20. The corresponding Fe K-edge EXAFS fitting parameters for (a) Fe-N-C and (b) Ni_7/Fe_3-N-C samples.

Table S1. EXAFS fitting parameters at the Ni K-edge for various samples

Sample	Shell	N [a]	R (Å) [b]	σ^2 (Å^2·10^{-3}) [c]	ΔE0 (eV) [d]	*R* factor (%)
Ni_7/Fe_3-N-C	Ni-N	4.5	1.84	9.2	-5.1	0.3
Ni-N-C	Ni -N	3.9	1.87	6.5	-5.9	0.7
	Ni -C	3.2	2.12	6.3	-1.6	

[a]*N*: coordination numbers; [b]*R*: bond distance; [c]σ^2: Debye-Waller factors; [d]ΔE_0: the inner potential correction. *R* factor: goodness of fit. *S*02 were set as 0.85/0.80 for Ni-N/Ni-C, which was obtained from the experimental EXAFS fit of reference FePc by fixing CN as the known crystallographic value and was fixed to all the samples.

Table S2. EXAFS fitting parameters at the Fe K-edge for various samples

Sample	Shell	N [a]	R (Å) [b]	σ^2 (Å^2·10^{-3}) [c]	ΔE0 (eV) [d]	*R* factor (%)
Ni_7/Fe_3-N-C	Fe-N(O)	4.8	1.98	8.9	-2.4	1.1
Fe-N-C	Fe-N	6.1	1.99	10.1	-3.3	0.3
	Fe-Fe	1.0	2.52	7.2	-1.5	

[a]*N*: coordination numbers; [b]*R*: bond distance; [c]σ^2: Debye-Waller factors; [d]ΔE_0: the inner potential correction. *R* factor: goodness of fit. *S*02 were set as 0.85/0.90 for Fe-N/Fe-Fe, which was obtained from the experimental EXAFS fit of reference FePc/Fe foil by fixing CN as the known crystallographic value and was fixed to all the samples.

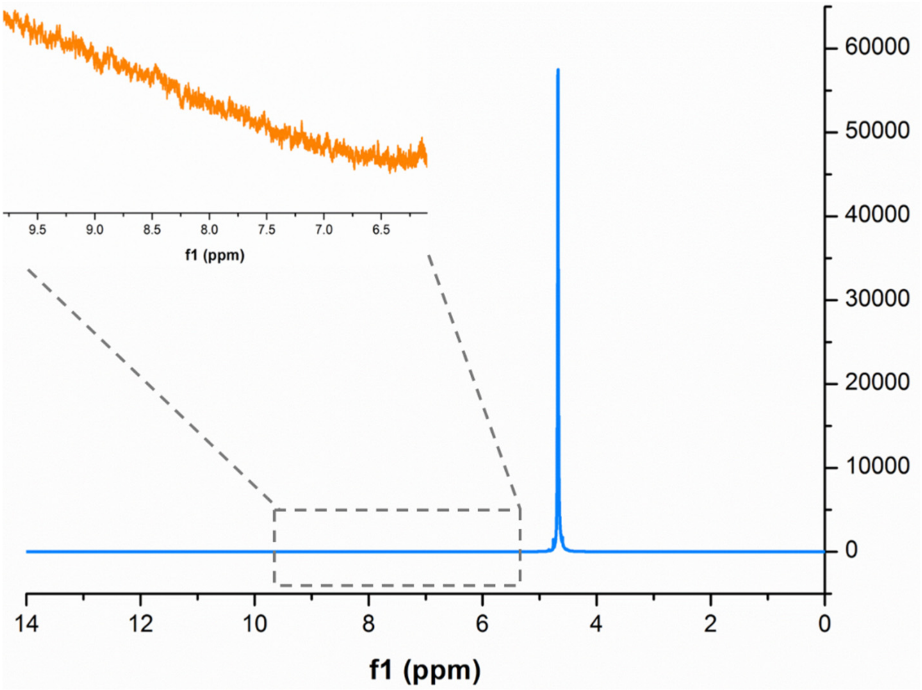

Fig. S21. The representative ^{1}H-NMR spectra of the electrolyte after electrolysis of −0.50 V for Ni_7/Fe_3-N-C in CO_2-saturated 0.5 M $NaHCO_3$ electrolyte for 30 h.

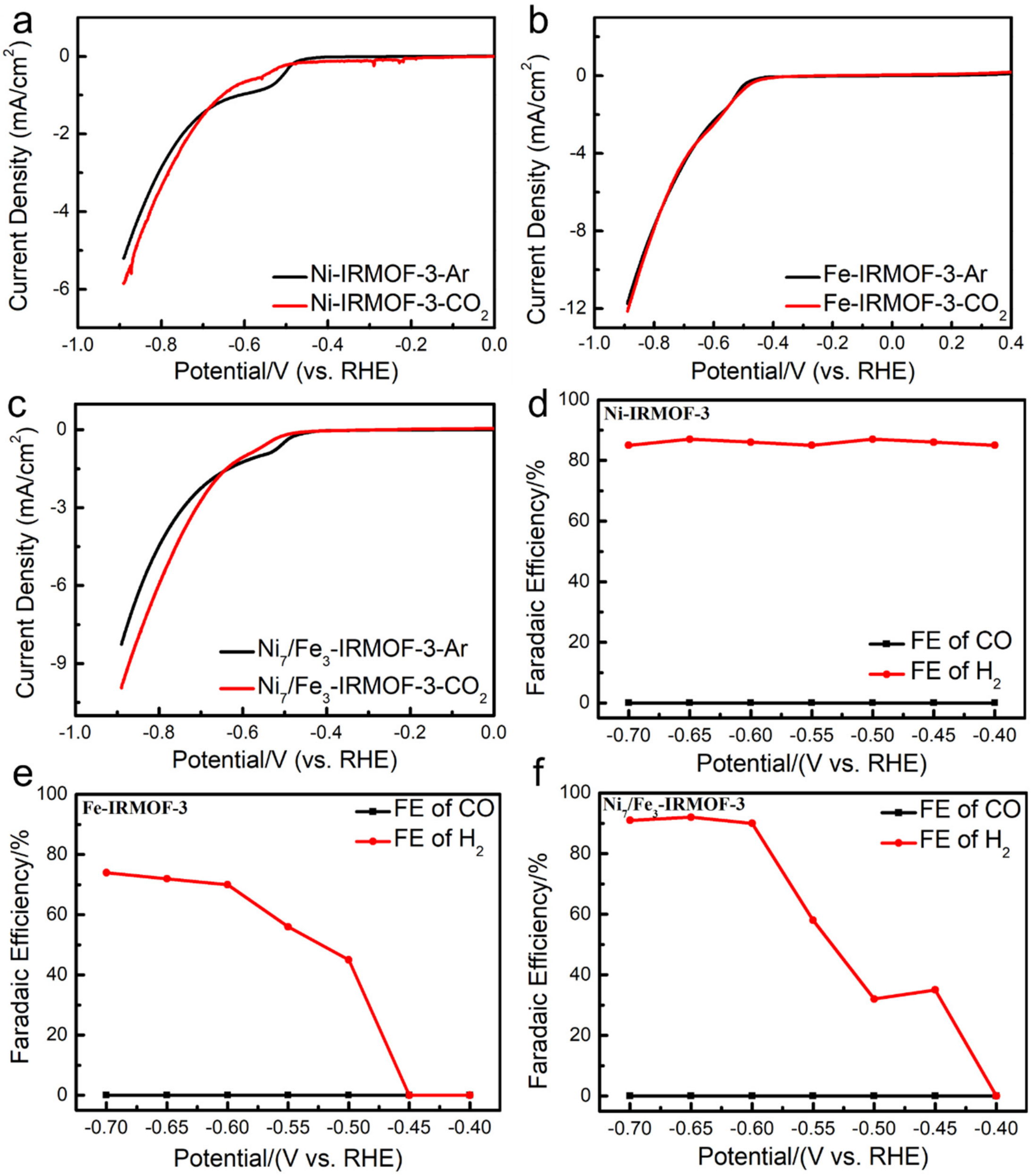

Fig. S22. LSV curves vs. RHE of (a) Ni-IRMOF-3, (b) Fe-IRMOF-3, and (c) Ni_7/Fe_3-IRMOF-3 obtained in Ar- or CO_2-saturated 0.5 M $NaHCO_3$ solution. FE of CO at various potentials and FE of H_2 at various potentials on (d) Ni-IRMOF-3, (e) Fe-IRMOF-3, (f) Ni_7/Fe_3-IRMOF-3.

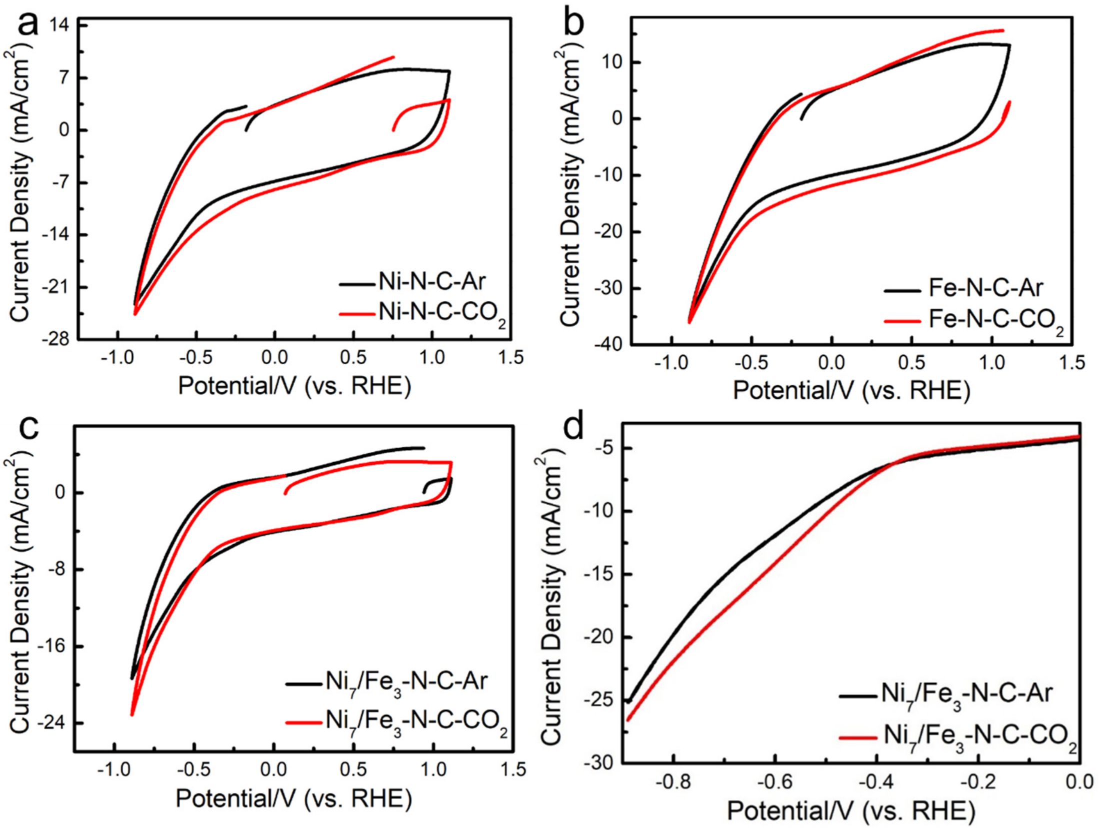

Fig. S23. CV curves vs. RHE of (a) Ni-N-C, (b) Fe-N-C, (c) Ni_7/Fe_3-N-C and (d) LSV curves vs. RHE of Ni_7/Fe_3-N-C obtained in Ar- or CO_2-saturated 0.5 M $NaHCO_3$ solution.

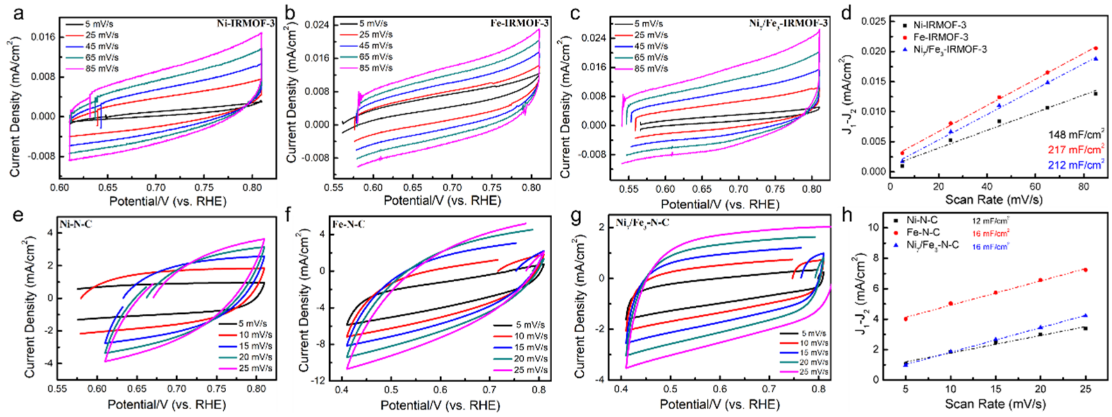

Fig. S24. Cyclic voltammograms curves for (a) Ni-IRMOF-3, (b) Fe-IRMOF-3, (c) Ni_7/Fe_3-IRMOF-3, (e) Ni-N-C, (f) Fe-N-C and (g) Ni_7/Fe_3-N-C. (d) Plots of the current density vs. scan rate for Ni-IRMOF-3, Fe-IRMOF-3 and Ni_7/Fe_3-IRMOF-3 electrodes. (h) Plots of the current density vs. scan rate for Ni-Ni-N-C, Fe-N-C and Ni_7/Fe_3-N-C electrodes.

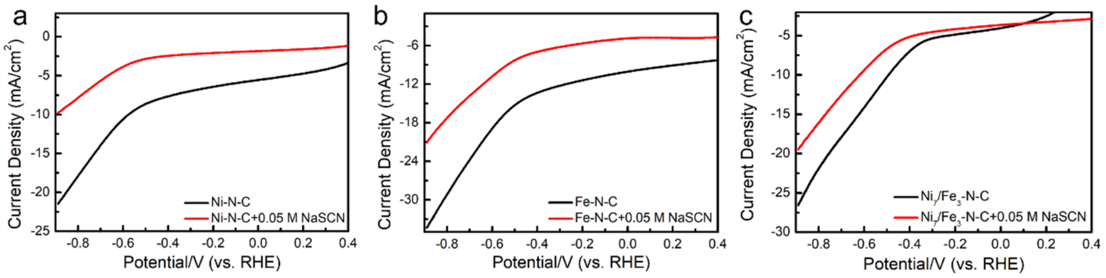

Fig. S25. Linear sweep voltammetry curves of (a) Ni-N-C, (b) Fe-N-C and (c) Ni_7/Fe_3-N-C with and without 0.05 M NaSCN.

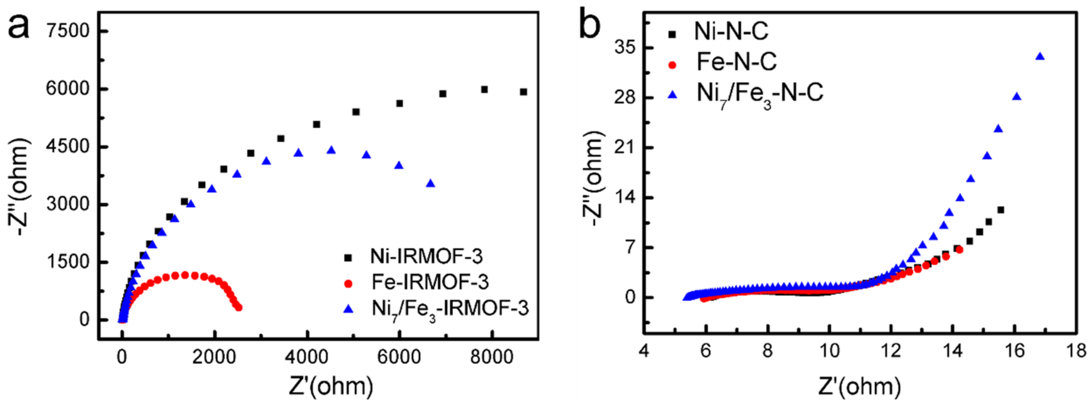

Fig. S26. Electrochemical impedance spectroscopy (EIS) of (a) Ni-IRMOF-3, Fe-IRMOF-3 and Ni_7/Fe_3-IRMOF-3, as well as (b) Ni-N-C, Fe-N-C and Ni_7/Fe_3-N-C.

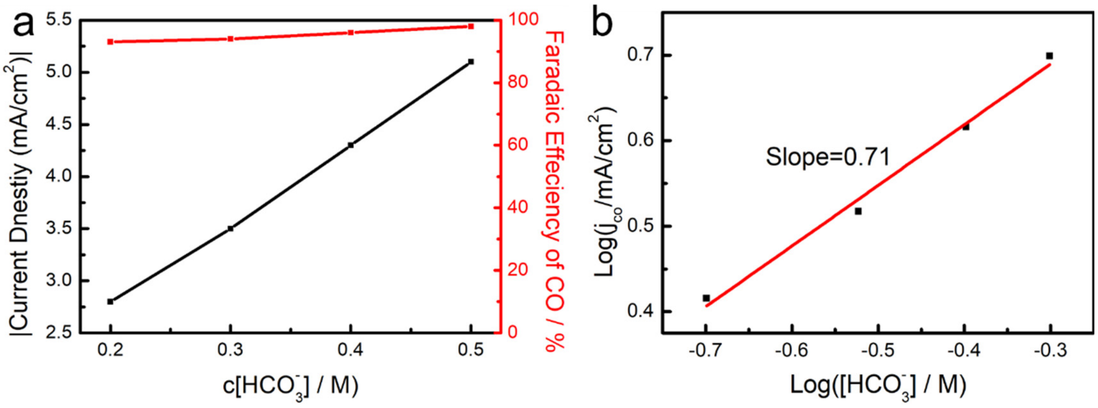

Figure S27. (a) Current density and FE of Ni_7/Fe_3-N-C at different $NaHCO_3$ concentration at a constant potential (−0.50 V vs. RHE). (b) Partial CO current density of Ni_7/Fe_3-N-C vs. $NaHCO_3$ concentration at −0.50 V vs. RHE.

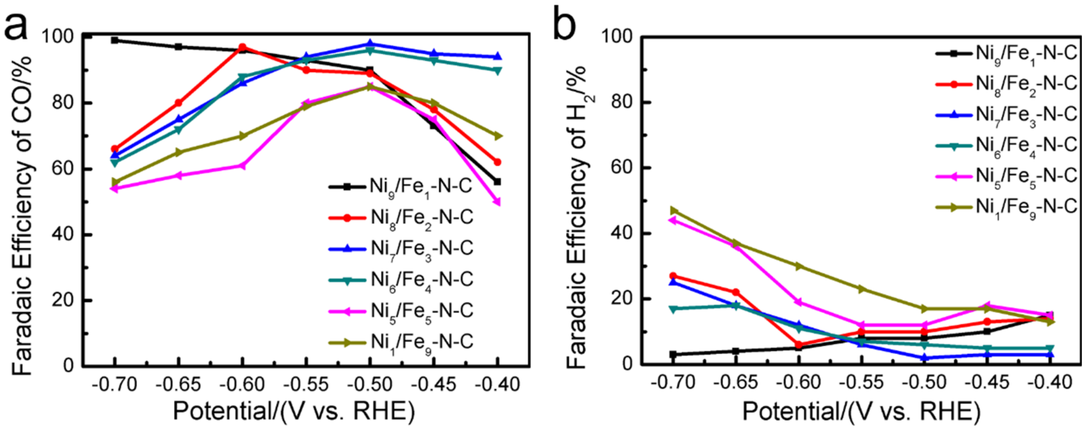

Fig. S28. (a) FE of CO and (b) FE of H_2 at various potentials on Ni_x/Fe_y-N-C.

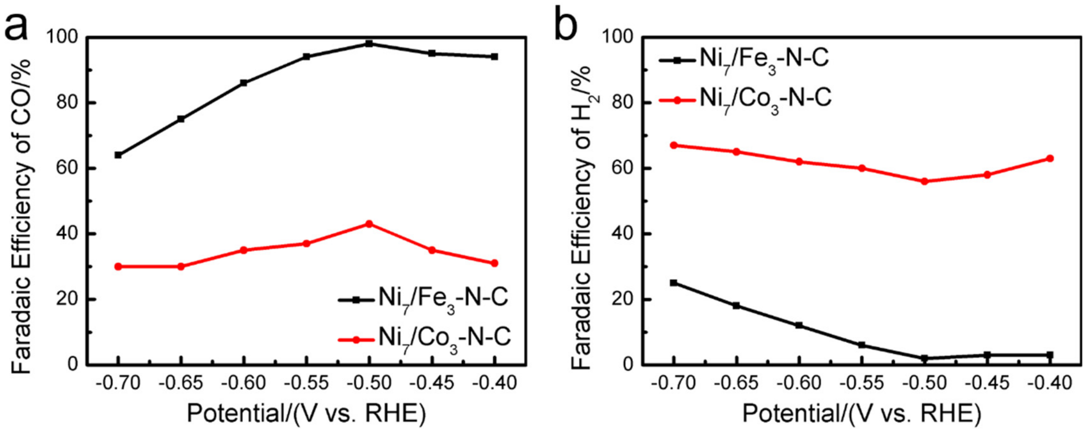

Fig. S29. (a) FE of CO and (b) FE of H_2 at various potentials on Ni_7/Fe_3-N-C and Ni_7/Co_3-N-C.

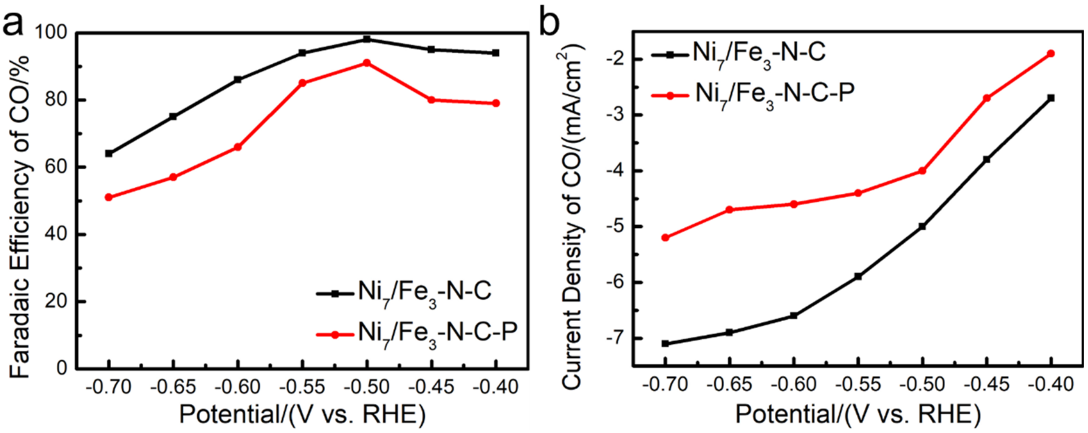

Fig. S30. (a) FE of CO at various potentials and (b) Current density for CO production on Ni_7/Fe_3-N-C and Ni_7/Fe_3-N-C-P.

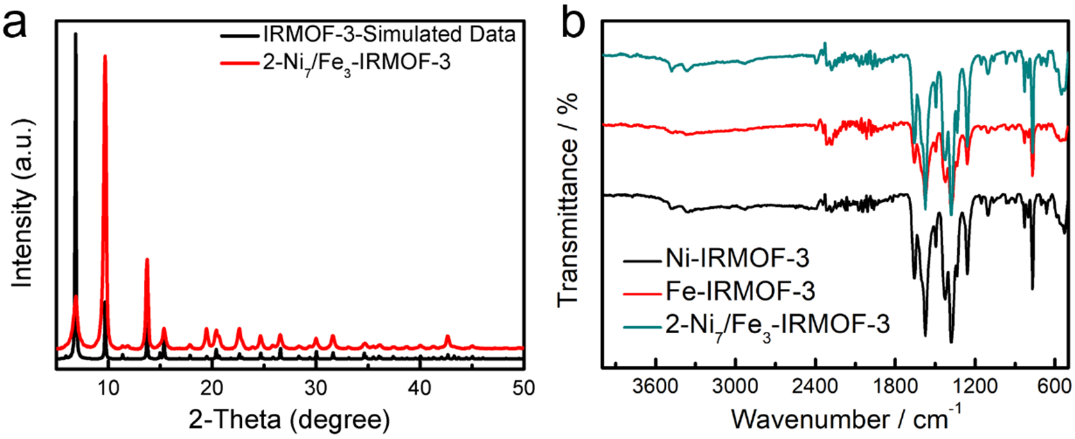

Fig. S31. (a) XRD patterns and (b) FTIR image of 2-Ni$_7$/Fe$_3$-IRMOF-3.

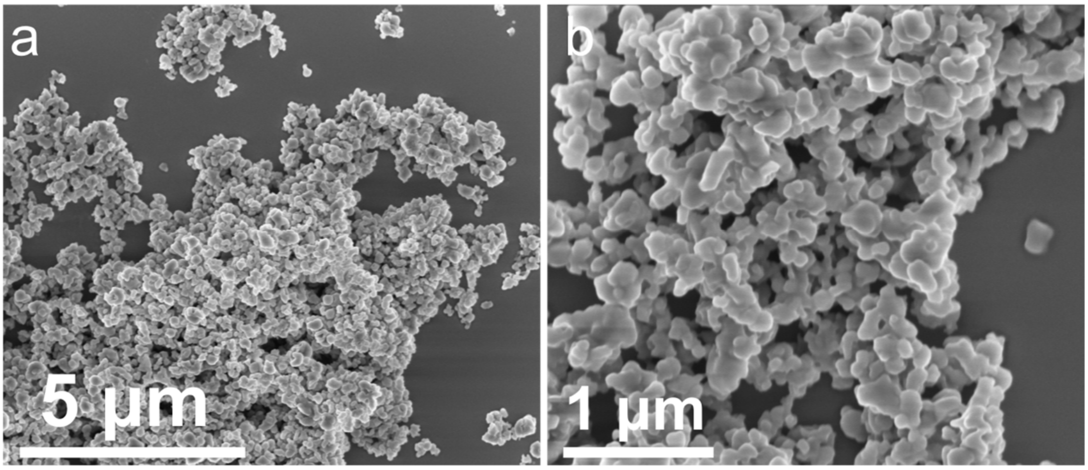

Fig. S32. SEM images of 2-Ni$_7$/Fe$_3$-IRMOF-3.

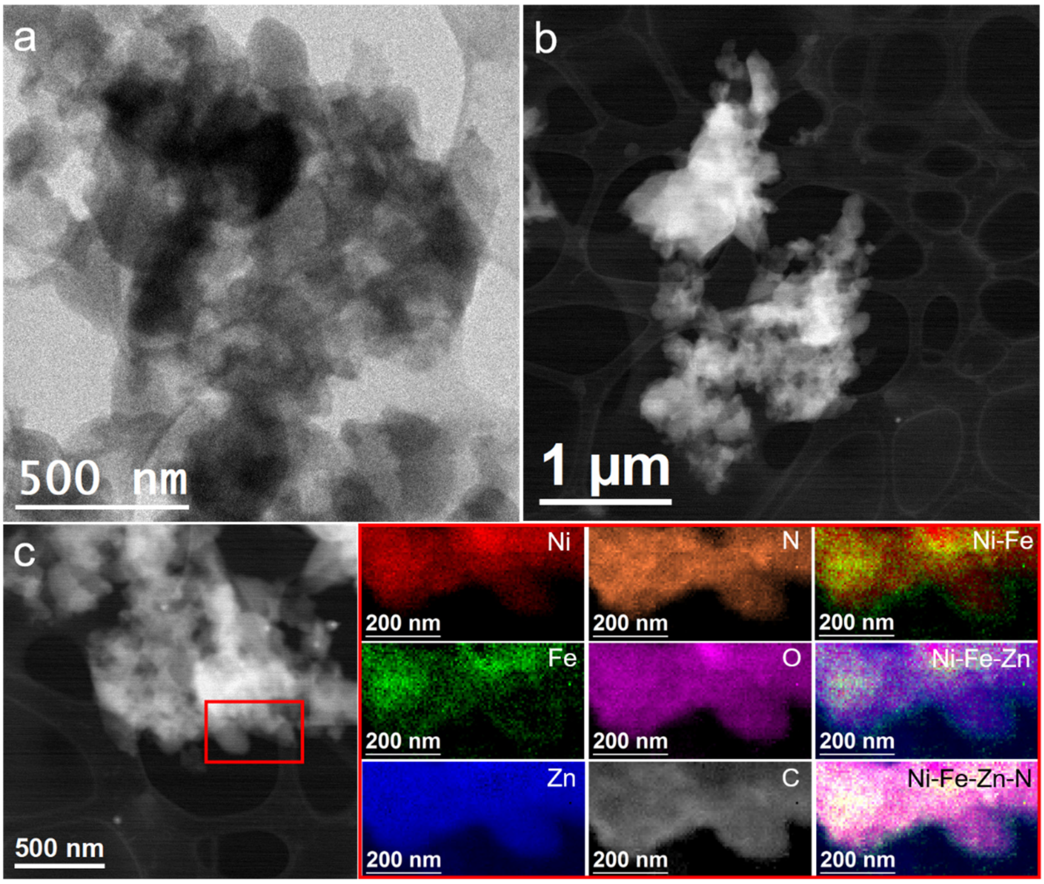

Fig. S33. (a) BF TEM, (b and c) HAADF STEM image of 2-Ni_7/Fe_3-IRMOF-3 and representative EELS chemical composition maps obtained from the red squared area of the STEM micrograph. Individual Ni $L_{2,3}$-edges at 855 eV (red), Fe $L_{2,3}$-edges at 708 eV (green), Zn $L_{2,3}$-edges at 1020 eV (blue), N K-edges at 401 eV (orange), O K-edges at 532 eV (pink) and C K-edges at 285 eV (grey) as well as composites of Ni-Fe, Ni-Fe-Zn and Ni-Fe-Zn-N.

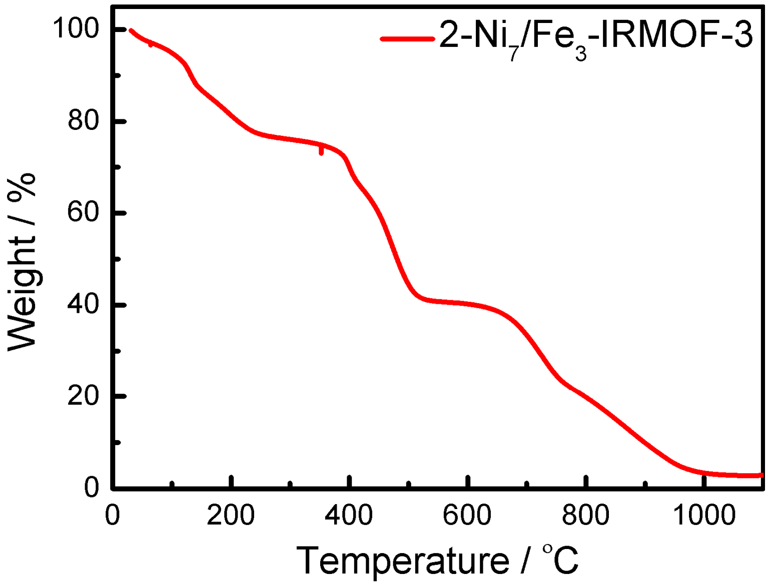

Fig. 34. TGA of 2-Ni$_7$/Fe$_3$-IRMOF-3.

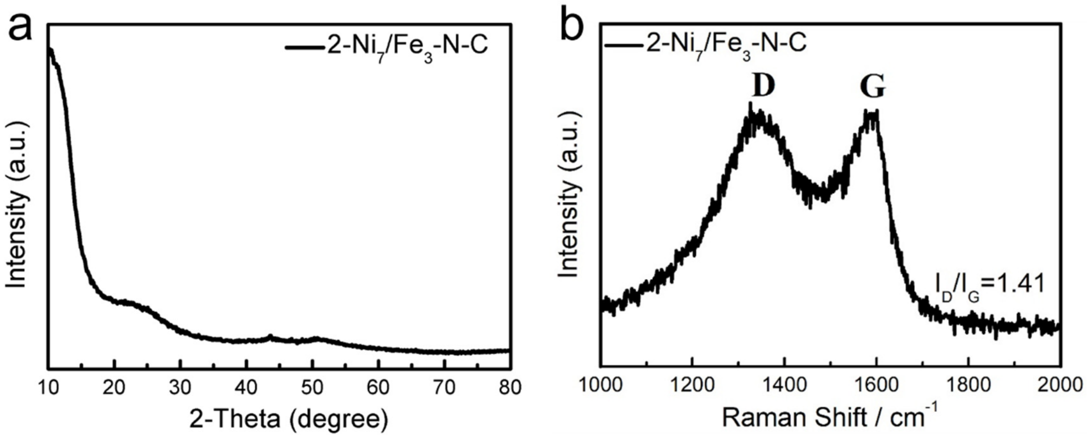

Fig. S35. (a) XRD patterns and (b) Raman spectra of 2-Ni_7/Fe_3-N-C.

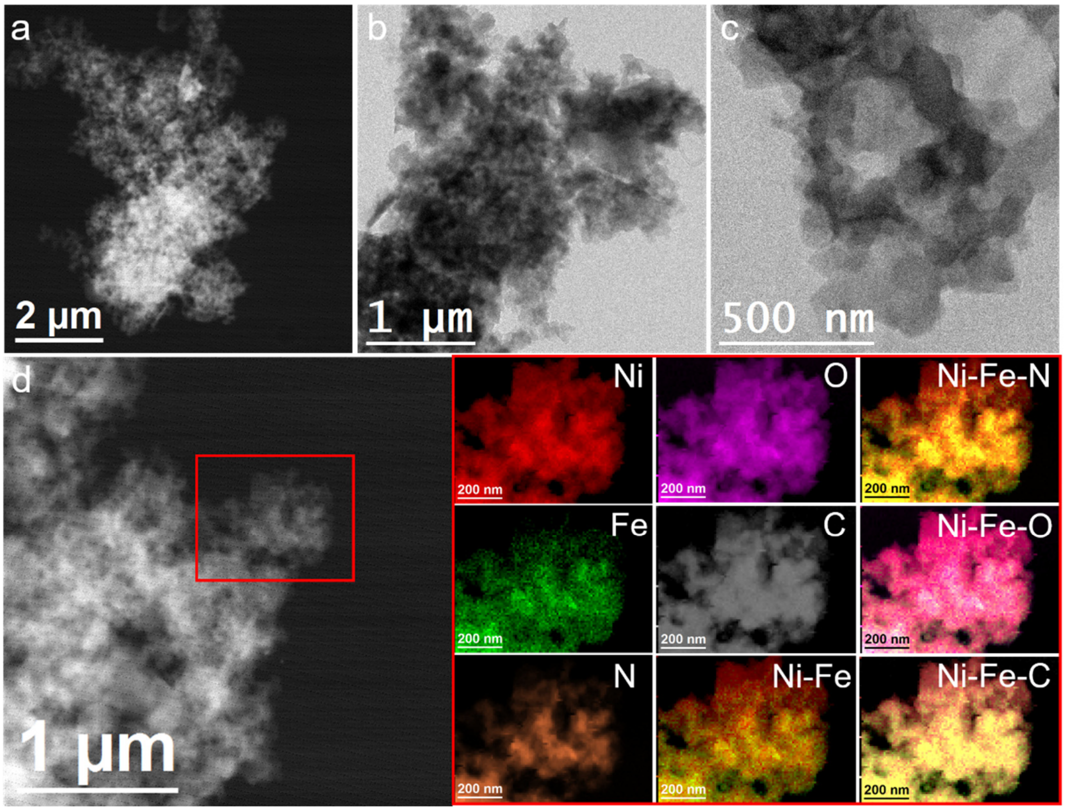

Fig. S36. (a) HAADF STEM, (b, c) BF TEM images of 2-Ni_7/Fe_3-N-C, (d) HAADF STEM image and representative EELS chemical composition maps obtained from the red squared area of the STEM micrograph. Individual Ni $L_{2,3}$-edges at 855 eV (red), Fe $L_{2,3}$-edges at 708 eV (green), N K-edges at 401 eV (orange), O K-edges at 532 eV (pink) and C K-edges at 285 eV (grey) as well as composites of Ni-Fe, Ni-Fe-N, Ni-Fe-O and Ni-Fe-C.

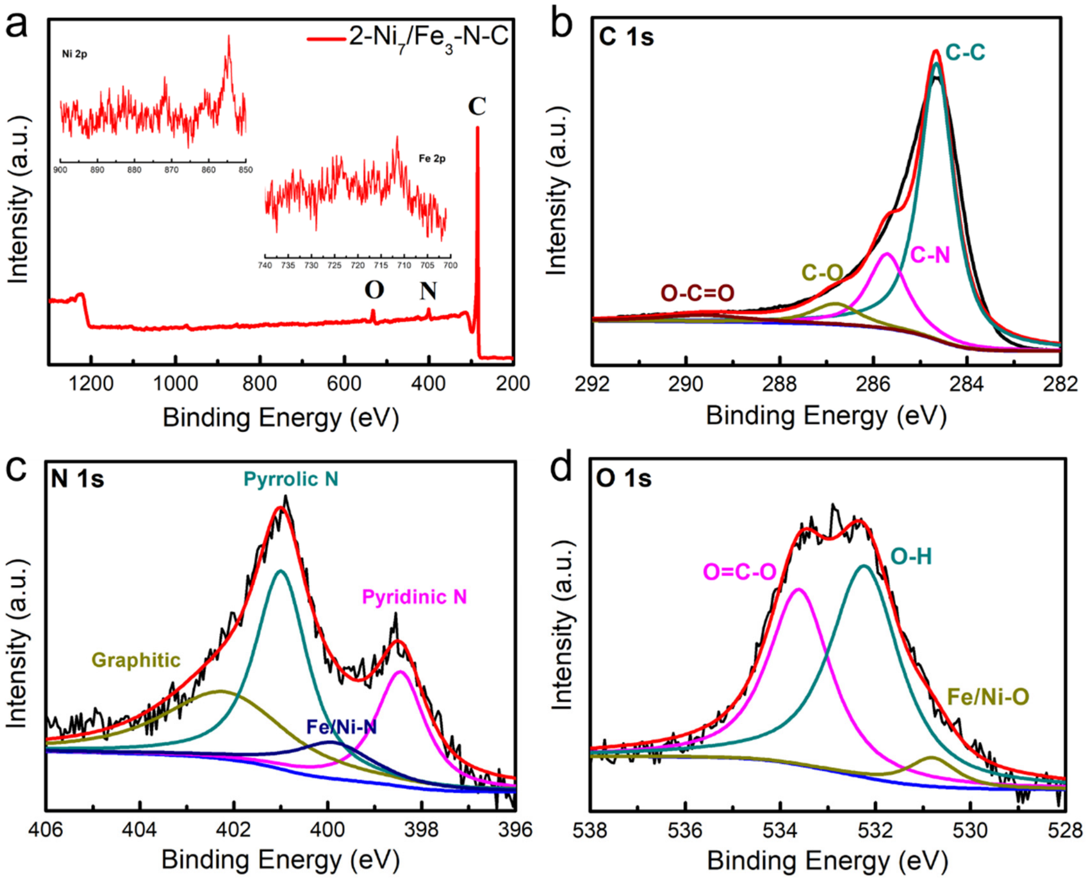

Fig. S37. XPS spectra for the (a) survey scan, (inset) Ni 2p and Fe 2p, (b) C 1s, (c) N 1s and (d) O 1s of 2-Ni_7/Fe_3-N-C.

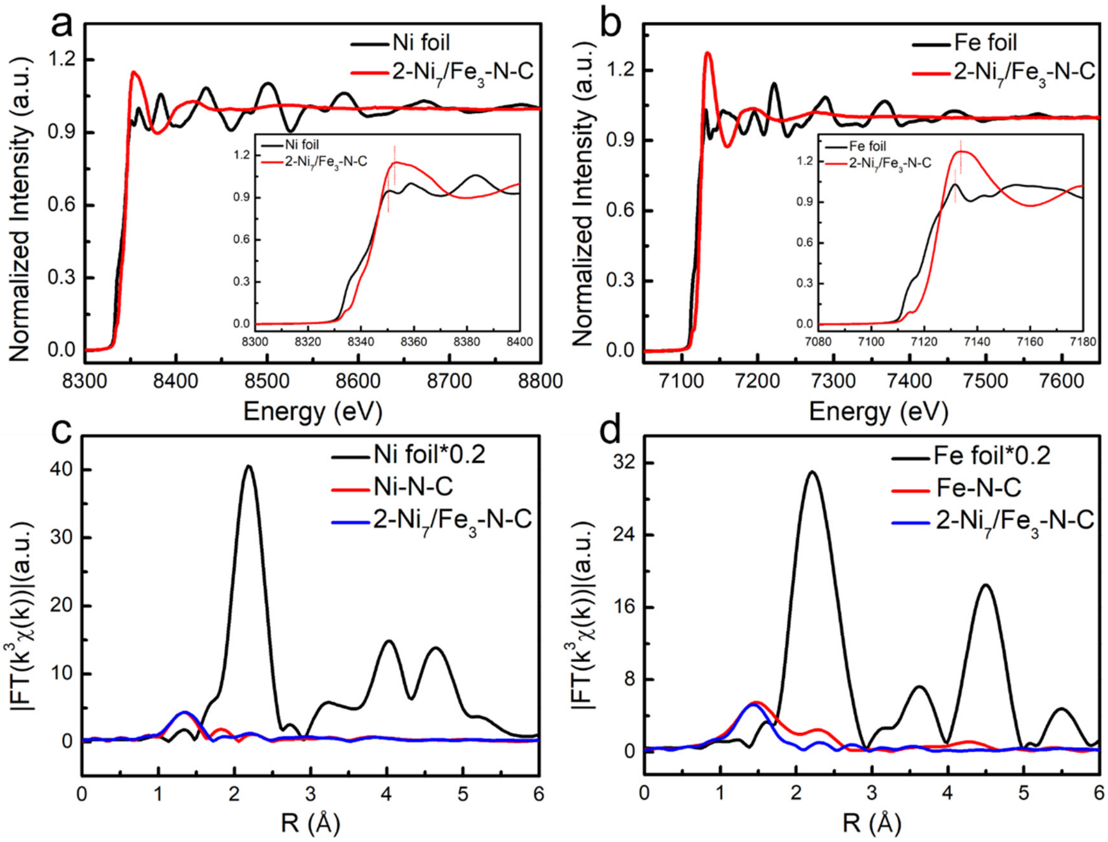

Fig. S38. (a) Ni K-edge XANES spectra of Ni foil and 2-Ni_7/Fe_3-N-C. (b) Fe K-edge XANES spectra of Fe foil and 2-Ni_7/Fe_3-N-C. (c and d) Fourier transformation of the EXAFS spectra at R space.

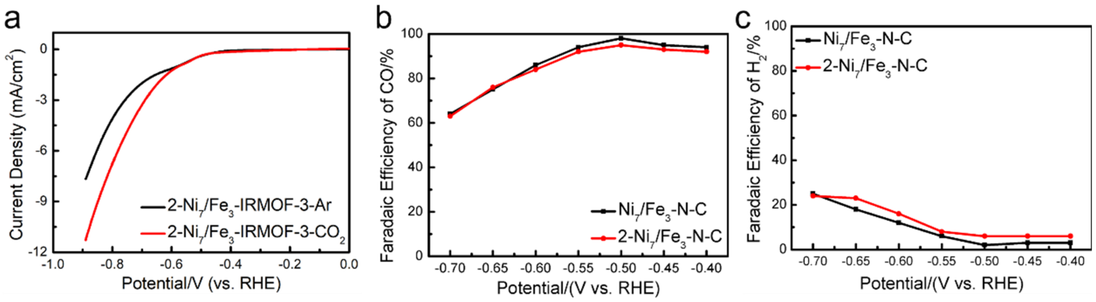

Fig. S39. (a) LSV of 2-Ni_7/Fe_3-N-C obtained in Ar- or CO_2-saturated 0.5 M $NaHCO_3$ solution. FE of (b) CO and (c) FE of H_2 at various potentials on Ni_7/Fe_3-N-C and 2-Ni_7/Fe_3-N-C.

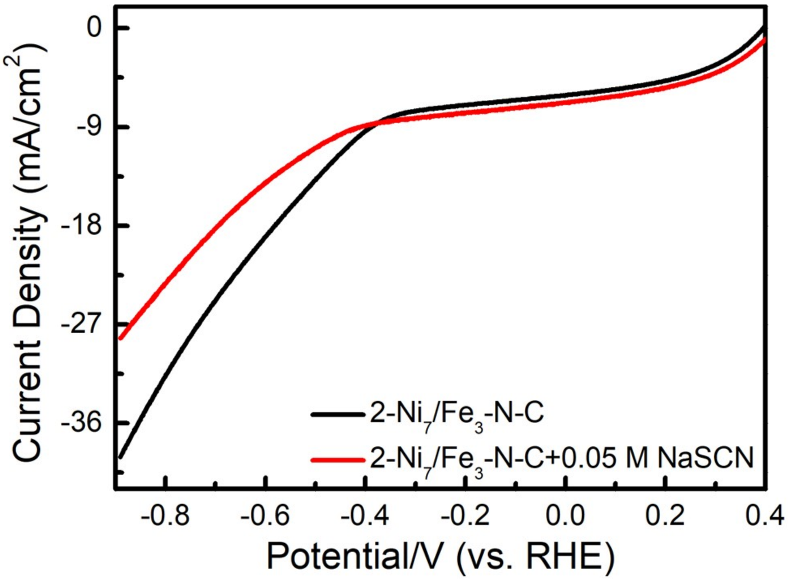

Fig. S40. Linear sweep voltammetry curves of 2-Ni_7/Fe_3-N-C with and without 0.05 M NaSCN.

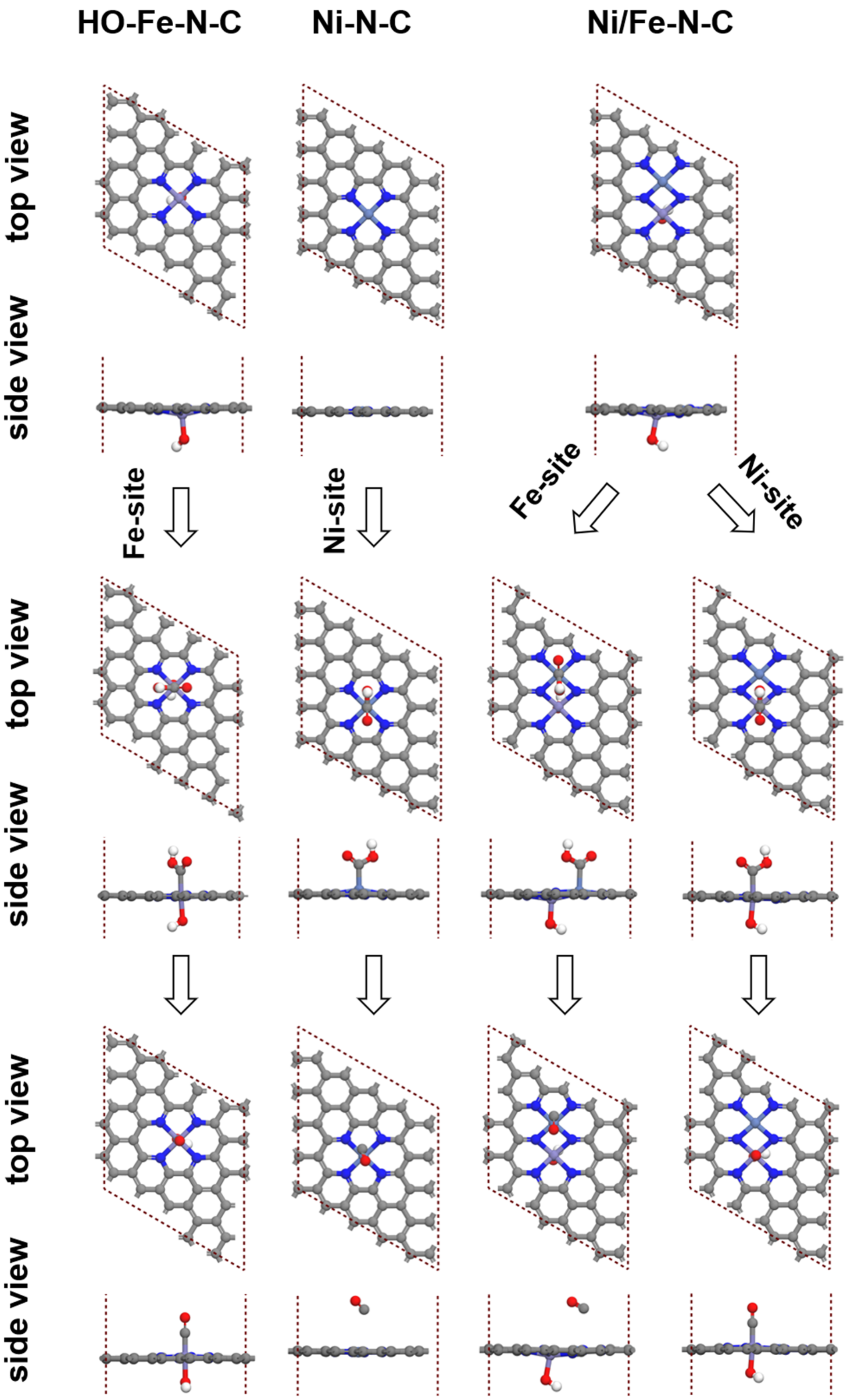

Fig. S41. The top view and side view of optimized adsorption configuration on simulated models (Ni, Fe, O, N and C atoms are represented in purple, cyan, red, blue and grey, respectively).

Table S3. Faradaic Efficiency (CO) of the reported single/double atom-based electrocatalysts for CO_2 electroreduction.

Catalyst	Product	FE(CO)	Potential	Reference
Fe-N-C	CO	93 %	−0.60 V vs. RHE	17
Fe-N-C	CO	81 %	−0.57 V vs. RHE	18
Fe-N-C	CO	93.5 %	−0.50 V vs. RHE	19
Fe-N-C	CO	93 %	−0.60 V vs. RHE	20
Fe-N-C	CO	80 %	−0.60 V vs. RHE	21
Fe-N-C	CO	92 %	−0.58 V vs. RHE	22
Fe-N-C	CO	64 %	−0.60 V vs. RHE	23
Fe-N-C	CO	95.47 %	−0.60 V vs. RHE	24
Fe-N_5-C	CO	97 %	−0.46 V vs. RHE	25
Fe-N-C	CO	95 %	−0.45 V vs. RHE	26
Ni-N-C	CO	99 %	−0.68 V vs. RHE	5
Ni-N-C	CO	71.9 %	−0.90 V vs. RHE	6
Ni-N-C	CO	95 %	−0.70 V vs. RHE	27
Ni-N-C	CO	99 %	−0.81 V vs. RHE	28
Ni-N-C	CO	96 %	−0.67 V vs. RHE	29
Ni-N-C	CO	96 %	−0.86 V vs. RHE	30
Ni-N-C	CO	95 %	−0.77 V vs. RHE	31
Ni-N-C	CO	91.2 %	−0.90 V vs. RHE	32
Ni-N-C	CO	97 %	−0.70 V vs. RHE	33
Ni-N-C	CO	95 %	−0.77 V vs. RHE	34
Ni-N-C	CO	99 %	−0.80 V vs. RHE	35
Ni-N-C	CO	94 %	−0.80 V vs. RHE	36
NiCo-N-C	CO	53 %	−0.60 V vs. RHE	37
Ni/Fe-N-C	CO	98 %	−0.70 V vs. RHE	38
Ni/Fe-N-C	CO	90 %	−0.65 V vs. RHE	39
Ni/Mn-C_3N_4-CNT	CO	90 %	−0.70 V vs. RHE	40
ZnCo-N-C	CO	93.2 %	−0.50 V vs. RHE	41
Ni-N-Co	CO	96.4 %	−0.48 V vs. RHE	42
Ni_7/Fe_3-N-C	**CO**	**98 %**	**−0.50 V vs. RHE**	**This work**

References

1. B. Ravel and M. Newville, *J. Synchrotron Radiat.*, 2005, **12**, 537-541.
2. H. Baumgartel, *Nachrichten aus Chemie, Technik und Laboratorium*, 1988, **36**, 650-650.
3. J. J. Rehr and R. C. Albers, *Rev. Modern Phys.*, 2000, **72**, 621-654.
4. T. Zhang, J. Du, P. Xi and C. Xu, *ACS Appl. Mater. Interfaces*, 2017, **9**, 362-370.
5. T. Zheng, K. Jiang, N. Ta, Y. Hu, J. Zeng, J. Liu and H. Wang, *Joule*, 2019, **3**, 265-278.
6. C. Zhao, X. Dai, T. Yao, W. Chen, X. Wang, J. Wang, J. Yang, S. Wei, Y. Wu and Y. Li, *J. Am. Chem. Soc.*, 2017, **139**, 8078-8081.
7. P. E. Blöchl, *Phys. Rev. B*, 1994, **50**, 17953-17979.
8. G. Kresse and J. Furthmüller, *Phys. Rev. B*, 1996, **54**, 11169-11186.
9. G. Kresse and J. Furthmüller, *Comput. Mater. Sci.*, 1996, **6**, 15-50.
10. G. Kresse and D. Joubert, *Phys. Rev. B*, 1999, **59**, 1758-1775.
11. J. Hafner, *J. Comput. Chem.*, 2008, **29**, 2044.
12. J. Wellendorff, K. T. Lundgaard, A. Møgelhøj, V. Petzold, D. D. Landis, J. K. Nørskov, T. Bligaard and K. W. Jacobsen, *Phys. Rev. B*, 2012, **85**, 235149.
13. F. Studt, M. Behrens, E. L. Kunkes, N. Thomas, S. Zander, A. Tarasov, J. Schumann, E. Frei, J. B. Varley, F. Abild-Pedersen, J. K. Nørskov and R. Schlögl, *ChemCatChem*, 2015, **7**, 1105-1111.
14. F. Studt, F. Abild-Pedersen, J. B. Varley and J. K. Nørskov, *Catal. Lett.*, 2013, **143**, 71-73.
15. R. Christensen, H. A. Hansen and T. Vegge, *Catal. Sci. Technol.*, 2015, **5**, 4946-4949.
16. A. A. Peterson, F. Abild-Pedersen, F. Studt, J. Rossmeisl and J. K. Nørskov, *Energy Environ. Sci.*, 2010, **3**, 1311-1315.
17. F. Pan, H. Zhang, K. Liu, D. Cullen, K. More, M. Wang, Z. Feng, G. Wang, G. Wu and Y. Li, *ACS Catal.*, 2018, **8**, 3116-3122.
18. X.-M. Hu, H. H. Hval, E. T. Bjerglund, K. J. Dalgaard, M. R. Madsen, M.-M. Pohl, E. Welter, P. Lamagni, K. B. Buhl, M. Bremholm, M. Beller, S. U. Pedersen, T. Skrydstrup and K. Daasbjerg, *ACS Catal.*, 2018, **8**, 6255-6264.
19. X. Qin, S. Zhu, F. Xiao, L. Zhang and M. Shao, *ACS Energy Lett.*, 2019, **4**, 1778-1783.
20. X. Li, S. Xi, L. Sun, S. Dou, Z. Huang, T. Su and X. Wang, *Adv. Sci.*, 2020, **7**, 2001545.
21. C. Zhang, S. Yang, J. Wu, M. Liu, S. Yazdi, M. Ren, J. Sha, J. Zhong, K. Nie, A. S. Jalilov, Z. Li, H. Li, B. I. Yakobson, Q. Wu, E. Ringe, H. Xu, P. M. Ajayan and J. M. Tour, *Adv. Energy Mate.*, 2018, **8**, 1703487.
22. Q. Zhang, H. Jiang, D. Niu, X. Zhang, S. Sun and S. Hu, *ChemistrySelect*, 2019, **4**, 4398-4406.
23. J. Zhao, J. Deng, J. Han, S. Imhanria, K. Chen and W. Wang, *Chem. Engineering J.*, 2020, **389**, 124323.
24. J. Tuo, Y. Lin, Y. Zhu, H. Jiang, Y. Li, L. Cheng, R. Pang, J. Shen, L. Song and C. Li, *Appl. Catal. B: Environ.*, 2020, **272**, 118960.
25. H. Zhang, J. Li, S. Xi, Y. Du, X. Hai, J. Wang, H. Xu, G. Wu, J. Zhang, J. Lu and J. Wang, *Angew. Chem. Int. Ed.*, 2019, **58**, 14871-14876.
26. J. Gu, C.-S. Hsu, L. Bai, H. M. Chen and X. Hu, *Science*, 2019, **364**, 1091-1094.
27. W. Xiong, H. Li, H. Wang, J. Yi, H. You, S. Zhang, Y. Hou, M. Cao, T. Zhang and R. Cao, *Small*, 2020, **16**, 2003943.
28. X. Li, W. Bi, M. Chen, Y. Sun, H. Ju, W. Yan, J. Zhu, X. Wu, W. Chu, C. Wu and Y. Xie, *J.*

Am. Chem. Soc., 2017, **139**, 14889-14892.

29. S. Yang, J. Zhang, L. Peng, M. Asgari, D. Stoian, I. Kochetygov, W. Luo, E. Oveisi, O. Trukhina, A. H. Clark, D. T. Sun and W. L. Queen, *Chem. Sci.*, 2020, **11**, 10991-10997.
30. Y. Lu, H. Wang, P. Yu, Y. Yuan, R. Shahbazian-Yassar, Y. Sheng, S. Wu, W. Tu, G. Liu, M. Kraft and R. Xu, *Nano Energy*, 2020, **77**, 105158.
31. S.-G. Han, D.-D. Ma, S.-H. Zhou, K. Zhang, W.-B. Wei, Y. Du, X.-T. Wu, Q. Xu, R. Zou and Q.-L. Zhu, *Appl. Catal. B: Environ.*, 2021, **283**, 119591.
32. C.-Z. Yuan, K. Liang, X.-M. Xia, Z. K. Yang, Y.-F. Jiang, T. Zhao, C. Lin, T.-Y. Cheang, S.-L. Zhong and A.-W. Xu, *Catal. Sci. Technology*, 2019, **9**, 3669-3674.
33. X. Yang, J. Cheng, B. Fang, X. Xuan, N. Liu, X. Yang and J. Zhou, *Nanoscale*, 2020, **12**, 18437-18445.
34. K. Jiang, S. Siahrostami, T. Zheng, Y. Hu, S. Hwang, E. Stavitski, Y. Peng, J. Dynes, M. Gangisetty, D. Su, K. Attenkofer and H. Wang, *Energy Environ. Sci.*, 2018, **11**, 893-903.
35. C. F. Wen, F. Mao, Y. Liu, X. Y. Zhang, H. Q. Fu, L. R. Zheng, P. F. Liu and H. G. Yang, *ACS Catal.*, 2020, **10**, 1086-1093.
36. X. Rong, H.-J. Wang, X.-L. Lu, R. Si and T.-B. Lu, *Angew. Chem. Int. Ed.*, 2020, **59**, 1961-1965.
37. Q. He, D. Liu, J. H. Lee, Y. Liu, Z. Xie, S. Hwang, S. Kattel, L. Song and J. G. Chen, *Angew. Chem. Int. Ed.*, 2020, **59**, 3033-3037.
38. W. Ren, X. Tan, W. Yang, C. Jia, S. Xu, K. Wang, S. C. Smith and C. Zhao, *Angew. Chem. Int. Ed.*, 2019, **58**, 6972-6976.
39. M. Zhang, Z. Hu, L. Gu, Q. Zhang, L. Zhang, Q. Song, W. Zhou and S. Hu, *Nano Res.*, 2020, **13**, 3206-3211.
40. C. Ding, C. Feng, Y. Mei, F. Liu, H. Wang, M. Dupuis and C. Li, *Appl. Catal. B: Environ.*, 2020, **268**, 118391.
41. W. Zhu, L. Zhang, S. Liu, A. Li, X. Yuan, C. Hu, G. Zhang, W. Deng, K. Zang, J. Luo, Y. Zhu, M. Gu, Z.-J. Zhao and J. Gong, *Angew. Chem. Int. Ed.*, 2020, **59**, 12664-12668.
42. J. Pei, T. Wang, R. Sui, X. Zhang, D. Zhou, F. Qin, X. Zhao, Q. Liu, W. Yan, J. Dong, L. Zheng, A. Li, J. Mao, W. Zhu, W. Chen and Z. Zhuang, *Energy Environ. Sci.*, 2021, DOI: 10.1039/D0EE03947K.

Institut Català de Nanociència i Nanotecnologia
Barcelona Institute of Science and Technology
CSIC

J. Arbiol
arbiol@icrea.cat www.gaen.cat

Prof. Dr. Jordi Arbiol
ICREA Professor and Group Leader
Catalan Institute of Nanoscience and Nanotechnology (ICN2), CSIC & BIST
Edifici ICN2, Campus UAB - 08193 Bellaterra (Barcelona) Spain
Tel: +34 937373654
Email: arbiol@icrea.cat
25th May 2021

Dear Editor-in-Chief of ***Energy & Environmental Science***,

It is my pleasure to submit our original manuscript entitled "**Quasi-Double-Star Nickel and Iron Active Sites for High-Efficient Carbon Dioxide Electroreduction**" to ***Energy & Environmental Science*** as a **Full paper**.

Ni-based single-atom catalysts (SACs) have a great potential to tackle the challenges in CO_2 reduction reaction (CO_2 RR) for generating CO because of their relatively high selectivity. However, the practical application is still limited by their high overpotentials (> 600 mV vs. RHE), which implies a higher consumption of energy to drive the CO_2 RR.

In the present work, we have combined the advantages of both Ni-N-C and Fe-N based catalysts to overcome this problem. On one side, Ni-N-C catalysts possess a rapid desorption of *CO ($CO^* \rightarrow CO + *$) due to the related weak bonding of CO, whereas on the other side, Fe-N active sites generally show a low overpotential for CO_2 RR because of the fast first proton-coupled electron transfer. In addition, we have shown that the presence of Fe adjacent to the Ni sites in a specific environment can lead to influence the electron density and configuration environment between both active sites, and thus facilitate the adsorption and desorption of intermediates in the CO_2 reduction process. In this work, we propose that a quasi-double star catalyst with the cooperation of close Fe and Ni active sites might act as a nano-reactor and significantly affect different reaction steps on the two separate (but close) active sites, and thus, boost both, the CO_2 RR activity and selectivity. In the following, we would like to highlight, four relevant issues addressed in the present manuscript about the designed double-star Ni/Fe catalyst:

1) **Successful fabrication of bimetallic single atom active sites**. We have prepared a bimetallic Ni/Fe catalyst composed of adjacent Ni and Fe active sites without Ni-Fe bonds through a simple pyrolysis of Ni and Fe co-doped Zn-based MOFs, delivering a high selectivity at a low overpotential during CO_2 RR.

2) **Formation of adjacent NiN_4 and HO-FeN_4 sites.** Based on previous publications, it has been shown that the FeN_4 active sites with oxygen-containing groups can induce a rapid CO* desorption and suppress the competitive HER, resulting in a much better CO_2 RR catalytic performance than that of FeN_4 sites without axial O ligand. However, it is a high challenge to introduce -OH subgroups into FeN_4 single atom catalysts due to their energetically unstable nature. Herein, by using simple oxygen and nitrogen-rich MOFs as sacrificial templates, instead of a simple N-rich ligand, we have successfully introduced in-situ axial bonded -OH subgroups on FeN_4 sites and locate them close to the formed NiN_4 sites.

3) **Enhanced CO_2 RR activity.** The optimized Ni_7/Fe_3-N-C catalyst showed an exclusive selectivity (a maximum FE (CO) of 98 %) at a low overpotential of 390 mV vs. RHE, which is better than those of previous reported Fe-based and Ni-based SACs (**Figure 1**) and other state-of-the-art double-atom catalysts (**Figure 2**).

4) **Computational insights unveiling the detailed reaction mechanism.** Via DFT calculations, we have

proved that regulating the catalytic CO_2 RR performance via adjacent Ni and Fe active sites in a bimetallic Ni/Fe-N-C catalyst can potentially break the activity benchmark of single metal counterparts because the neighboring Ni and Fe active sites not only function in synergy to decrease the reaction barrier for the formation of COOH* and desorption of CO* in comparison to their single metal counterparts, but also prevent the undesired hydrogen evolution reaction (HER).

Overall, we believe this work will be of interest to the general ***Energy & Environmental Science*** audience as it opens a new field for the development of high-performance catalysts with adjacent double-metal single atoms to regulate the binding energy of different intermediates during the adsorption and desorption processes, thus, influencing different reaction steps over two active sites towards CO_2 RR to achieve excellent catalytic performances. Thank you very much in advance for considering the present manuscript.

Yours sincerely,
Prof. Dr. Jordi Arbiol

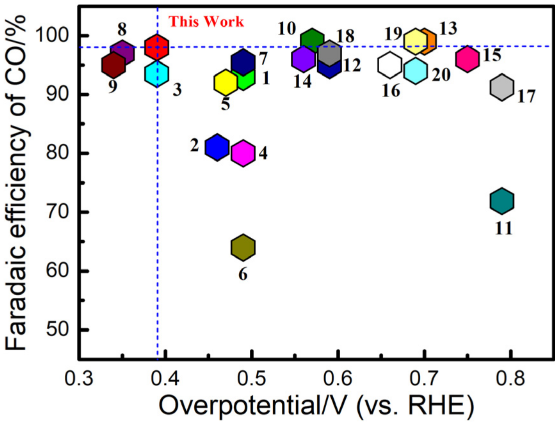

Figure 1. Faradaic Efficiency (CO) of the reported Fe-based and Ni-based single atom electrocatalysts for CO_2 electroreduction.

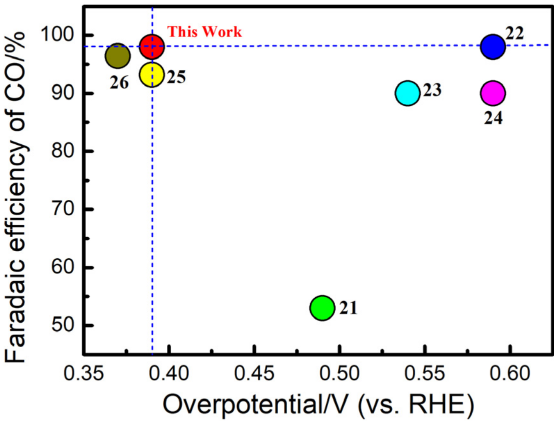

Figure 2. Faradaic Efficiency (CO) of the reported double-atom electrocatalysts for CO_2 electroreduction.

References

1. F. Pan, H. Zhang, K. Liu, D. Cullen, K. More, M. Wang, Z. Feng, G. Wang, G. Wu and Y. Li, *ACS Catal.*, 2018, **8**, 3116-3122.
2. X.-M. Hu, H. H. Hval, E. T. Bjerglund, K. J. Dalgaard, M. R. Madsen, M.-M. Pohl, E. Welter, P. Lamagni, K. B. Buhl, M. Bremholm, M. Beller, S. U. Pedersen, T. Skrydstrup and K. Daasbjerg, *ACS Catal.*, 2018, **8**, 6255-6264.
3. X. Qin, S. Zhu, F. Xiao, L. Zhang and M. Shao, *ACS Energy Lett.*, 2019, **4**, 1778-1783.
4. C. Zhang, S. Yang, J. Wu, M. Liu, S. Yazdi, M. Ren, J. Sha, J. Zhong, K. Nie, A. S. Jalilov, Z. Li, H. Li, B. I. Yakobson, Q. Wu, E. Ringe, H. Xu, P. M. Ajayan and J. M. Tour, *Adv. Energy Mater.*, 2018, **8**, 1703487.
5. Q. Zhang, H. Jiang, D. Niu, X. Zhang, S. Sun and S. Hu, *ChemistrySelect*, 2019, **4**, 4398-4406.
6. J. Zhao, J. Deng, J. Han, S. Imhanria, K. Chen and W. Wang, *Chem. Engineering J.*, 2020, **389**, 124323.
7. J. Tuo, Y. Lin, Y. Zhu, H. Jiang, Y. Li, L. Cheng, R. Pang, J. Shen, L. Song and C. Li, *Appl. Catal. B: Environ.*,

2020, **272**, 118960.

8. H. Zhang, J. Li, S. Xi, Y. Du, X. Hai, J. Wang, H. Xu, G. Wu, J. Zhang, J. Lu and J. Wang, *Angew. Chem. Int. Ed.*, 2019, **58**, 14871-14876.
9. J. Gu, C.-S. Hsu, L. Bai, H. M. Chen and X. Hu, *Science*, 2019, **364**, 1091-1094.
10. T. Zheng, K. Jiang, N. Ta, Y. Hu, J. Zeng, J. Liu and H. Wang, *Joule*, 2019, **3**, 265-278.
11. C. Zhao, X. Dai, T. Yao, W. Chen, X. Wang, J. Wang, J. Yang, S. Wei, Y. Wu and Y. Li, *J. Am. Chem. Soc.*, 2017, **139**, 8078-8081.
12. W. Xiong, H. Li, H. Wang, J. Yi, H. You, S. Zhang, Y. Hou, M. Cao, T. Zhang and R. Cao, *Small*, 2020, **16**, 2003943.
13. X. Li, W. Bi, M. Chen, Y. Sun, H. Ju, W. Yan, J. Zhu, X. Wu, W. Chu, C. Wu and Y. Xie, *J. Am. Chem. Soc.*, 2017, **139**, 14889-14892.
14. S. Yang, J. Zhang, L. Peng, M. Asgari, D. Stoian, I. Kochetygov, W. Luo, E. Oveisi, O. Trukhina, A. H. Clark, D. T. Sun and W. L. Queen, *Chem. Sci.*, 2020, **11**, 10991-10997.
15. Y. Lu, H. Wang, P. Yu, Y. Yuan, R. Shahbazian-Yassar, Y. Sheng, S. Wu, W. Tu, G. Liu, M. Kraft and R. Xu, *Nano Energy*, 2020, **77**, 105158.
16. S.-G. Han, D.-D. Ma, S.-H. Zhou, K. Zhang, W.-B. Wei, Y. Du, X.-T. Wu, Q. Xu, R. Zou and Q.-L. Zhu, *Appl. Catal. B: Environ.*, 2021, **283**, 119591.
17. C.-Z. Yuan, K. Liang, X.-M. Xia, Z. K. Yang, Y.-F. Jiang, T. Zhao, C. Lin, T.-Y. Cheang, S.-L. Zhong and A.-W. Xu, *Catal. Sci. Technol.*, 2019, **9**, 3669-3674.
18. X. Yang, J. Cheng, B. Fang, X. Xuan, N. Liu, X. Yang and J. Zhou, *Nanoscale*, 2020, **12**, 18437-18445.
19. C. F. Wen, F. Mao, Y. Liu, X. Y. Zhang, H. Q. Fu, L. R. Zheng, P. F. Liu and H. G. Yang, *ACS Catal.*, 2020, **10**, 1086-1093.
20. X. Rong, H.-J. Wang, X.-L. Lu, R. Si and T.-B. Lu, *Angew. Chem. Int. Ed.*, 2020, **59**, 1961-1965.
21. Q. He, D. Liu, J. H. Lee, Y. Liu, Z. Xie, S. Hwang, S. Kattel, L. Song and J. G. Chen, *Angew. Chem. Int. Ed.*, 2020, **59**, 3033-3037.
22. W. Ren, X. Tan, W. Yang, C. Jia, S. Xu, K. Wang, S. C. Smith and C. Zhao, *Angew. Chem. Int. Ed.*, 2019, **58**, 6972-6976.
23. M. Zhang, Z. Hu, L. Gu, Q. Zhang, L. Zhang, Q. Song, W. Zhou and S. Hu, *Nano Res.*, 2020, **13**, 3206-3211.
24. C. Ding, C. Feng, Y. Mei, F. Liu, H. Wang, M. Dupuis and C. Li, *Appl. Catal. B: Environ.*, 2020, **268**, 118391.
25. W. Zhu, L. Zhang, S. Liu, A. Li, X. Yuan, C. Hu, G. Zhang, W. Deng, K. Zang, J. Luo, Y. Zhu, M. Gu, Z.-J. Zhao and J. Gong, *Angew. Chem. Int. Ed.*, 2020, **59**, 12664-12668.
26. J. Pei, T. Wang, R. Sui, X. Zhang, D. Zhou, F. Qin, X. Zhao, Q. Liu, W. Yan, J. Dong, L. Zheng, A. Li, J. Mao, W. Zhu, W. Chen and Z. Zhuang, *Energy Environ. Sci.*, 2021, DOI: 10.1039/D0EE03947K.

Broader Context

Electrochemical conversion of CO_2 powered by renewable energy to useful feedstocks is considered as an elegant solution to achieve the carbon cycle. Previous research has shown that transition metal-nitrogen-carbon (M-N-C) based materials are one of the most high-efficient electrocatalysts to transfer CO_2 to CO, bridging the gap between homogenous and heterogenous catalysts. Nevertheless, the electrocatalytic efficiencies of M-N-C based catalysts are significantly influenced by the selected transition metal (M). Typically, faradaic efficiency (FE) of most of Fe-N-C catalysts is less than 80 %, while almost all Ni-N-C catalysts have shown a high FE(CO) > 90 %. However, compared to Fe-N-C materials, those based on Ni-N-C normally exhibit higher overpotential, which represents higher driving force needed in the reaction, and thus, higher energy consumption. Considering both selectivity and activity, it is thus a huge challenge for single metal catalysts to achieve high FE(CO), while maintaining a low overpotential, which are the conditions essentially required for practical applications. In light of this, we have developed a quasi-double-star catalyst composed of nickel and iron single atom active sites, which not only significantly obtains an excellent FE(CO) but also maintains a low overpotential. This work opens a new way of employing the catalysts with adjacent double-metal single atoms to regulate the local environment between two active sites to achieve excellent catalytic performances.